JGR Space Physics

RESEARCH ARTICLE
10.1029/2021JA029777

Modeling Inner Proton Belt Variability at Energies 1 to 10 MeV Using BAS-PRO

Alexander R. Lozinski[1,2], Richard B. Horne[1], Sarah A. Glauert[1], Giulio Del Zanna[2], and Seth G. Claudepierre[3,4]

[1]British Antarctic Survey, Cambridge, UK, [2]Department of Applied Mathematics and Theoretical Physics, University of Cambridge, Cambridge, UK, [3]Space Sciences Department, The Aerospace Corporation, El Segundo, CA, USA, [4]Department of Atmospheric and Oceanic Sciences, UCLA, Los Angeles, CA, USA

Key Points:

- Uncertainty in proton D_{LL} can lead to several orders of magnitude difference in modeled steady state phase space density at $\mu = 20$ MeV/G
- Transition from solar maximum to minimum drives a significant increase in flux of 7.5 MeV equatorial protons at $L = 1.3$
- Anisotropy of proton pitch angle distributions at $L < 1.5$ shows either an increase or decrease toward higher L depending on D_{LL}

Correspondence to:

A. R. Lozinski,
alezin33@bas.ac.uk

Citation:

Lozinski, A. R., Horne, R. B., Glauert, S. A., Del Zanna, G., & Claudepierre, S. G. (2021). Modeling inner proton belt variability at energies 1 to 10 MeV using BAS-PRO. *Journal of Geophysical Research: Space Physics*, *126*, e2021JA029777. https://doi.org/10.1029/2021JA029777

Received 9 JUL 2021
Accepted 17 NOV 2021

Abstract Geomagnetically trapped protons forming Earth's proton radiation belt pose a hazard to orbiting spacecraft. In particular, solar cell degradation is caused by non-ionising collisions with protons at energies of several megaelectron volts (MeV), which can shorten mission lifespan. Dynamic enhancements in trapped proton flux following solar energetic particle events have been observed to last several months, and there is a strong need for physics-based modeling to predict the impact on spacecraft. However, modeling proton belt variability at this energy is challenging because radial diffusion coefficients are not well constrained. We address this by using the British Antarctic Survey proton belt model BAS-PRO to perform 3D simulations of the proton belt in the region $1.15 \leq L \leq 2$ from 2014 to 2018. The model is driven by measurements from the Radiation Belt Storm Probes Ion Composition Experiment and Magnetic Electron Ion Spectrometer instruments carried by the Van Allen Probe satellites. To investigate sensitivity, simulations are repeated for three different sets of proton radial diffusion coefficients D_{LL} taken from previous literature. Comparing the time evolution of each result, we find that solar cycle variability can drive up to a ~75% increase in 7.5 MeV flux at $L = 1.3$ over four years due to the increased importance of collisional loss at low energies. We also show how the anisotropy of proton pitch angle distributions varies with L and energy, depending on D_{LL}. However we find that phase space density can vary by three orders of magnitude at $L = 1.4$ and $\mu = 20$ MeV/G due to uncertainty in D_{LL}, highlighting the need to better constrain proton D_{LL} at low energy.

1. Introduction

The proton radiation belt is formed by protons with energies from several hundred kiloelectron volts (keV) up to hundreds of megaelectron volts (MeV) that orbit Earth along closed drift shells under the influence of the geomagnetic field. The three adiabatic invariants associated with gyration, bounce and drift motion are stable for a trapped particle, but may nevertheless be altered by a variety of processes leading to a finite lifetime. The proton belt at $L \lesssim 1.5$ tends to be shielded from time-variation of the geomagnetic field and so exhibits variability over long timescales of years to decades (Selesnick & Albert, 2019). At $L \sim 2$, variation in MeV flux nominally occurs on timescales of a year or so (Albert & Ginet, 1998), and at $L \gtrsim 2$ the proton belt may exhibit rapid variability due to geomagnetic disturbances. The radial profile of flux extends up to $L \sim 3.5$ at tens of MeV (e.g., Selesnick et al., 2014). The proton belt is therefore a challenging environment to model due to complex processes with a wide range of timescales applying over different coordinates of the trapped population.

Irradiation by trapped proton flux in the 1–20 MeV range is a primary cause of solar cell degradation for spacecraft traversing the proton belt, and a key factor influencing mission lifetime (Jenkins et al., 2014; Miyake et al., 2014). Predicting variability is therefore of practical importance for mission planning and operations, and could be achieved by incorporating data in real-time to forecast the exposure of satellites using physics-based models.

A key goal is to model the effect of electromagnetic field perturbations, which scatter particles across the field to neighboring drift shells and modify the third invariant. This requires the perturbation to occur over a small fraction of the drift period, and be asymmetric along the drift orbit (dependent on local time, Parker, 1960). Calculating the resulting motion of particles requires that perturbations in the field are known, but this is usually not practical for simulations relying on spacecraft data. Therefore, the time evolution of the particle distribution is modeled as subject to radial diffusion, as repeated perturbations cause the smoothing of gradients in proton phase space density as a function of magnetic L shell.

In theoretical work by Fälthammar (1965), the radial diffusion coefficient D_{LL} is formulated as the contribution of magnetic and electrostatic terms corresponding to different categories of perturbations. The magnetic term is often assumed to have a L^{10} dependence and decreases by up to ∼90% with decreasing equatorial pitch angle (Figure 3, Walt, 1971), whilst the electrostatic term varies with L^6 and is nearly independent of pitch angle (see review by Lejosne & Kollmann, 2020). Analytical expressions for D_{LL} by Lejosne (2019) include an inverse energy dependence, which has been previously demonstrated for electrons by modeling asymmetric field perturbations to derive D_{LL} analytically (see Figure 8, Lejosne et al., 2013). For protons, an energy-dependence is sometimes inferred empirically by works that choose D_{LL} to match results against spacecraft measurements of flux (i.e., Kovtyukh, 2016; Lozinski et al., 2021). However, the dependencies of proton D_{LL} are not well constrained in general, especially at $\lesssim$10 MeV where data is mostly unavailable.

The strong L dependence of D_{LL} means variations in MeV proton phase space density at low altitude ($L \lesssim 1.3$) are mostly driven by coulomb collisional loss, whereby free and bound electrons in the atmosphere, ionosphere and plasmasphere decelerate protons and reduce the first invariant μ (see Section II.2, Schulz & Lanzerotti, 1974). During solar maximum the atmosphere undergoes thermal expansion from increased extreme ultraviolet radiation (Fuller-Rowell et al., 2004). At fixed altitude in the radiation belts, this leads to higher density and therefore higher loss. Li et al. (2020) show this effect, plotting cyclical variations in proton flux near ∼40 MeV lagging behind changes in sunspot number, with a delay of hundreds of days just below $L = 1.2$ for equatorial particles. The relatively short timescales for variation indicate how trapped flux levels quickly rebalance changes in loss rather than conserve a previous state, in contrast to higher altitudes ($L \sim 1.6$) where radial diffusion controls variability over decades. However, at $L \gtrsim 2$, months long enhancements in proton belt flux have been recorded forming over ∼day timescales or less (Hudson et al., 1995; Lorentzen et al., 2002) due to trapping of incoming solar energetic particles (SEPs, see Kress et al., 2004, 2005). The radiation environment of satellites orbiting at $L \lesssim 2$ may therefore be subject to long term increases, driven by solar cycle or magnetic activity, where little data is available for monitoring.

In this work, we introduce the physics-based British Antarctic Survey proton belt model BAS-PRO, and use it to investigate the variability in ∼MeV proton phase space density at $1.15 \leq L \leq 2$ as a function of the three adiabatic invariants μ, K and L. To drive the model, we construct a dynamic outer boundary at $L = 2$ using proton flux data down to 0.7 MeV from the Radiation Belt Storm Probes Ion Composition Experiment (RBSPICE) and Magnetic Electron Ion Spectrometer (MagEIS) instruments on the Van Allen Probes mission (Blake et al., 2013; Mitchell et al., 2013). This data, described in Section 2, allows us to model variability over the period from January 2014 to March 2018. The model includes up to date evaluations of key source and loss processes governing the proton radiation belt in this region, including coulomb collisional loss and the cosmic ray albedo neutron decay (CRAND) source. We discuss modeling these processes in Section 3. In Section 4 we present results of a dynamic model run initialized from steady state for three sets of D_{LL} values taken from literature which exhibit various energy dependence, in order to highlight the sensitivity of results to this parameter. Finally, in Section 5, we discuss several features of these results. In particular, by showing the sensitivity to D_{LL} at low energies relevant for satellite solar cell degradation, we show a key practical impact of uncertainty in D_{LL}, and suggest more data is needed in the 1–20 MeV range to help constrain model parameters.

2. Proton Data

The Van Allen Probes pair of satellites (formerly known as the Radiation Belt Storm Probes, RBSP) were launched into elliptical orbit (∼600 km pergiee to ∼5.8R_E apogee) at 10° inclination on 30 August 2012 (Kessel et al., 2013). This work makes use of proton flux measurements collected by three instruments on board: the RBSPICE (Mitchell et al., 2013); the MagEIS (Blake et al., 2013); and the Relativistic Electron-Proton Telescope (REPT, Baker et al., 2012). At $L < 2$, certain measurements were contaminated by the unintended counting of electrons and higher energy protons. Therefore, processed data from all three instruments were combined to derive a spectrum at $L = 2$, the innermost region where this interference could be avoided. This section describes processing of RBSPICE and MagEIS measurements from Van Allen Probe B (RBSP-B) to derive ∼0.7–10 MeV proton flux from January 2014 to March 2018. Proton flux data at >19 MeV shown by Selesnick and Albert (2019), based on REPT measurements and covering the same period, was then used to extend the spectrum.

2.1. RBSPICE Measurements up to 1 MeV

2.1.1. Processing

The RBSPICE instrument measures ions from ~20 keV to several MeV. The type of data collected by the instrument sensor, and subsequently the data product generated, depends on the selected "hardware mode" at any given time. The availability of RBSPICE data products is therefore determined in part by which hardware modes were enabled at the time of data collection. We investigated the data availability from several products and found that extracting proton flux measurements at $L = 2$ over the model period was only feasible via the Ion Species High Energy Resolution Low Time Resolution (ISRHELT) product measuring ion spectra (Manweiler & Mull, 2017). However, despite its better availability, ISRHELT measurements are susceptible to electron contamination in certain regions due in part to the reduced accuracy of the hardware mode and, in addition, there is no discernment between ion species. This section describes the processing steps performed on ISRHELT data, and these two potential caveats are addressed in more detail throughout Section 2.1.2.

ISRHELT data is contained within the level 3 Common Data Format (CDF) files obtainable online at http://rbspiceb.ftecs.com/Level_3/ISRHELT/. This data (from Van Allen Probe B) was used to derive a time series of equatorial pitch angle distributions for each energy channel over the modelling period, as described below.

The CDF files provide proton differential unidirectional flux as a 3D array of values, with dimensions epoch, energy channel and telescope. There were six telescopes recording simultaneously, and each measurement of flux was taken in the instantaneous look direction of the corresponding telescope, rotating with the spacecraft. To allow for angular resolution of measurements, the CDF files also provide a 2D array of the telescope look directions in terms of local pitch angle, with dimensions epoch and telescope number. In order to capture variability at sufficient time resolution, the modelling period was first split into intervals six days long. Within each interval, data was then preprocessed according to the following steps: (a) the Python interface to IRBEM provided by the spacepy package (Morley et al., 2011) was used to calculate B/B_e (the ratio of local magnetic field strength to magnetic field strength at the equator along the local field line) at each measurement epoch, using the IGRF internal and Olson-Pfitzer quiet external magnetic field (Alken et al., 2021; Olson & Pfitzer, 1982); (b) the 2D array of telescope look directions was converted from local pitch angle α to equatorial pitch angle α_{eq} using the well-known relation

$$\frac{\sin^2(\alpha)}{B} = \frac{\sin^2(\alpha_{eq})}{B_e} \tag{1}$$

derived from conservation of the first invariant; (c) values of equatorial pitch angle were placed in one of 15 equally spaced bins spanning 0°–180° and of width $\Delta\alpha_{eq} = 12°$, with the first bin center at $\alpha_{eq} = 6°$; (d) each flux measurement was associated with an equatorial pitch angle bin via the recording telescope's look direction, and a cadence was applied to average the flux measurements in each bin across one minute intervals, resulting in a 4D array of flux with dimensions of time (at the centers of each one minute interval), energy channel, telescope and equatorial pitch angle bin; (e) for a given L, data outside $L \pm 0.02$ were filtered out using the spacecraft L location at each epoch provided within the CDF files.

Using this method, we examined the equatorial pitch angle distribution of a given energy, formed by one minute-averaged flux measurements collected across the six day period for which data was extracted. Measurements from the first telescope were ignored because they were found to cover only a narrow range in equatorial pitch angle. This was due to the telescope being centered close to the spacecraft spin axis and showing little spin modulation. Measurements from the five remaining telescopes were combined, and the equatorial pitch angle distributions at each energy were fitted using the function

$$j = A\sin^n(\alpha_{eq}) + c \tag{2}$$

where j is unidirectional flux at equatorial pitch angle α_{eq}, and A, n and c are the fitting parameters. By repeating the above process at each six day interval over the modeling period, the time series of fitted data for each instrument channel was derived.

Figure 1, left side of panel a, shows an example fitted pitch angle distribution at $L = 2$ from early June 2014 in the 0.69 MeV channel of ISRHELT, with the different colors corresponding to one minute-averaged flux

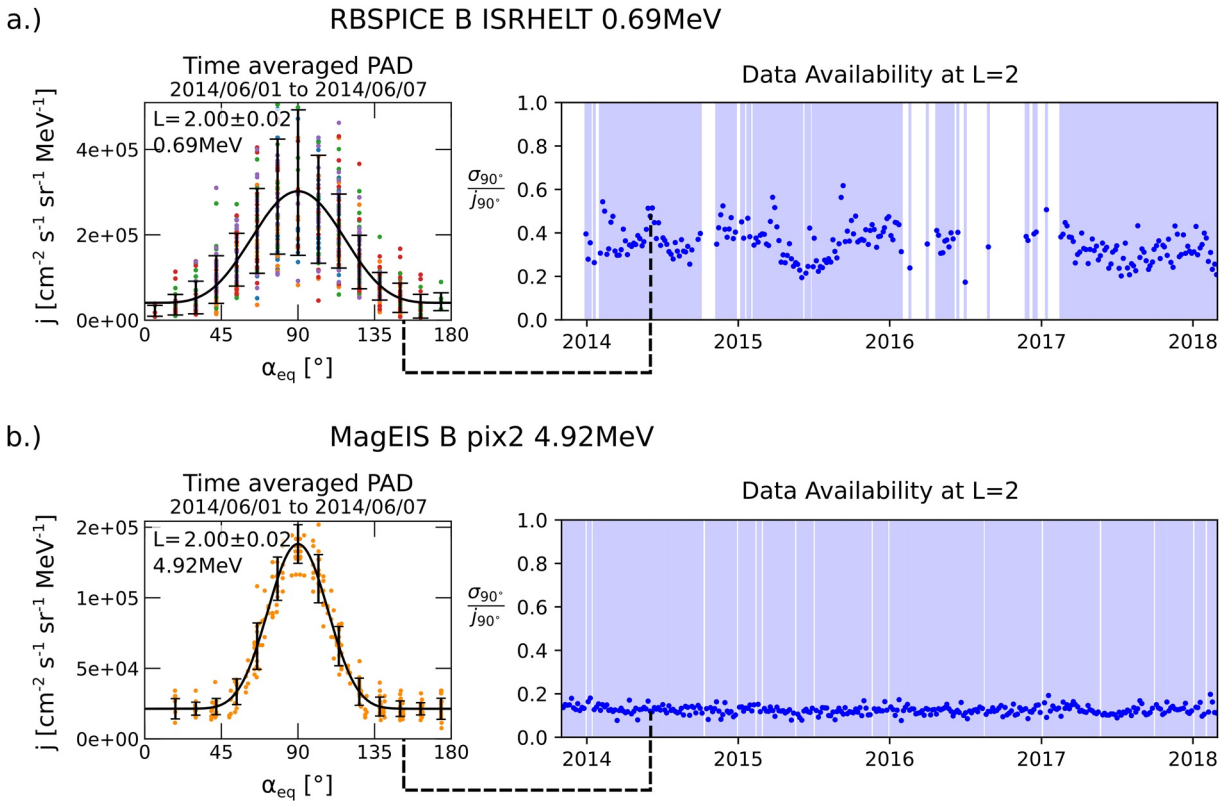

Figure 1. Summary of the data availability and quality of fit for preprocessed pitch angle distributions given by the Radiation Belt Storm Probes Ion Composition Experiment Ion Species High Energy Resolution Low Time data (panel a) and Magnetic Electron Ion Spectrometer pix2 data (panel b). Equatorial pitch angle distributions fitted using Equation 2 are shown on the left, along with the standard deviation of flux in each pitch angle bin. On the right, the ratio between the standard deviation in 90° flux measurements versus the mean flux value is shown for fitted pitch angle distributions at six day intervals at $L = 2$. White unshaded regions indicate a lack of data.

measurements taken by different telescopes. The standard deviations of the one minute-averaged fluxes in each pitch angle bin are shown by the black bars in Figure 1 and indicate data variability as well as reliability. Non-zero flux at loss cone pitch angles was assumed to be a consequence of insufficient angular resolution of the measurements rather than penetrating background, because the telescope look directions given in the CDF files represent the center of a few degrees range in local pitch angle, and were then binned after being converted to equatorial pitch angle as part of preprocessing, leading to some loss of precision. Some channels exhibit high standard deviations depending on the date and region. To give an overall sense of data availability and quality, Figure 1, right side of panel a, shows the ratio of the standard deviation to the absolute flux value in the 90° bin, taken from fits to the data at $L = 2$ over each time interval. Periods where data is unavailable are left unshaded (white). This plot corresponds to the 0.69 MeV channel but shows results representative for all channels of ISRHELT used in the study. Data is generally useable at $L = 2$ where the standard deviation of flux is $\lesssim$50% of the bin average.

2.1.2. Data Issues and Validation

The ISRHELT data product was collected using the "energy" mode of the RBSPICE instrument. In this mode, incident particle energy is measured by ion solid state detectors. However, there is no magnet in the RBSPICE detector to sweep out electrons, and so ISRHELT measurements may record the arrival of both species leading to contamination of ion flux. Another useful product from RBSPICE is the Time of Flight by Energy Ion Species Rates (TOFxEIon), which also provides flux of ions. However, in the hardware mode used for TOFxEIon, "time of flight" data is collected whereby a microchannel plate detects secondary electrons produced by the passage of an ion through two thin foils prior to the solid state detector, allowing detector counts to be validated as ions (Mitchell et al., 2013).

There are only a few short periods of time over which the TOFxEIon product is available down to $L = 2$, nevertheless they allowed a comparison to be made against ISRHELT. The susceptibility of ISRHELT data to electron contamination was therefore tested by preprocessing the TOFxEIon measurements using a similar method, and comparing the datasets at $L \geq 2$ over several months from April to mid-August 2017. When comparing 90° differential flux at $L = 2$ over this period, we found a very good agreement in the fitted flux distributions in the 0.84 and 0.93 MeV channels between instruments, and a reasonable (within factor of 2) agreement for the 0.63 and 0.76 MeV channels. Electron contamination issues in TOFxEIon data were not expected due to the time of flight data providing better accuracy, suggesting that ISRHELT was also not subject to major electron contamination in our region of interest. It was assumed that protons dominate the ion population in the region of interest, and therefore that ISRHELT and TOFxEIon ion measurements represent protons.

To continue checking for electron contamination, the fitted pitch angle distributions derived for ISRHELT (Section 2.1.1) were compared at different altitudes. When examining the radial profile of 90° flux versus L in energy channels up to 1 MeV, we found two peaks in some low energy channels. A peak at high altitude ($L > 3$) was expected, given the nominal distribution of flux according to previous measurements (i.e., Figure 5 of Stassinopoulos & Raymond, 1988). However, channels at 0.52 MeV and below exhibited a secondary flux peak at $L < 2$ which interfered with measurements at $L = 2$. These features were attributed to interference at $\lesssim$0.5 MeV, possibly from electrons. Finally, the energy spectrum at $L = 2$ derived from the fitted pitch angle distributions was found to show increasing flux with increasing energy, starting from the 1.85 and 2.03 MeV channels. This leads to a factor of ∼2 disagreement compared with the 2.05 MeV channel on MagEIS pix2 (see Section 2.2.1), and suggests that ISRHELT data at $\gtrsim$2 MeV may also be unreliable. Therefore, our use of RBSPICE ISRHELT data was limited to the six energy channels covering 0.69–1.13 MeV at $L = 2$, where no signs of contamination were found.

2.2. MagEIS Measurements up to 10 MeV

2.2.1. Processing

There are four MagEIS instruments on each Van Allen Probe. The "low" and "medium" energy units are electron spectrometers and do not measure ions. The "high" unit electron spectrometer also houses an ion range telescope with three silicon detectors. On Van Allen Probe B, ∼2–20 MeV protons are measured by the 2500-micron detector in this arrangement (Blake et al., 2013). This data is accessible via the "FPDU_pix2" variable in the Level 3 RBSP-B CDF files available online at the RBSP-ECT Science & Data Portal (https://rbsp-ect.newmexicoconsortium.org/data_pub/rbspb/). The excellent data continuity of "pix2" data over the modeling period allowed RBSPICE data to be supplemented with these higher energy measurements. However, as pix2 data was collected by a separate instrument, different processing steps were required as described below. Different contamination issues also arose, addressed in Section 2.2.2, but were comparatively minor.

The CDF files provide a 3D array of differential unidirectional flux with dimensions epoch, local pitch angle and energy channel. Local pitch angle is in terms of 15 equally spaced bins spanning 0°–180° and of width $\Delta\alpha_{eq} = 12°$, with the first bin center at $\alpha_{eq} = 6°$. A time series of equatorial pitch angle distributions was derived for each energy channel by splitting the modeling period into six day long intervals (the same as used to process RBSPICE ISRHELT data). Preprocessing the data was somewhat simpler because measurements of the full local pitch angle distribution were available at each epoch. Within each interval, the method used to preprocess data was as follows: (a) B/B_e was calculated at each epoch using Equation 1, again using the IGRF internal and Olson-Pfitzer quiet external magnetic field via spacepy; (b) local pitch angles at the center of each of the 15 bins were mapped to equatorial pitch angle at each epoch, and the mapped values stored directly (not re-binned) so that flux values in the 3D array were associated with equatorial pitch angle; (c) for a given L, data outside $L \pm 0.02$ were filtered out using the spacecraft L from the CDF files. This method resulted in every observation of flux within the six day interval being associated with equatorial pitch angle. Equation 2 was then used to fit an average distribution over all observations, and the process was repeated for each six day interval over the modeling period.

Figure 1, left side of panel b, shows an example fitted pitch angle distribution at $L = 2$ from early June 2014 in the 4.92 MeV channel. The standard deviations of flux are calculated across the distribution by binning observations in equatorial pitch angle, using the same 15 bins used to specify local pitch angle in the CDF file. The standard deviations are shown by the black bars in Figure 1. Compared with the standard deviations shown for ISRHELT

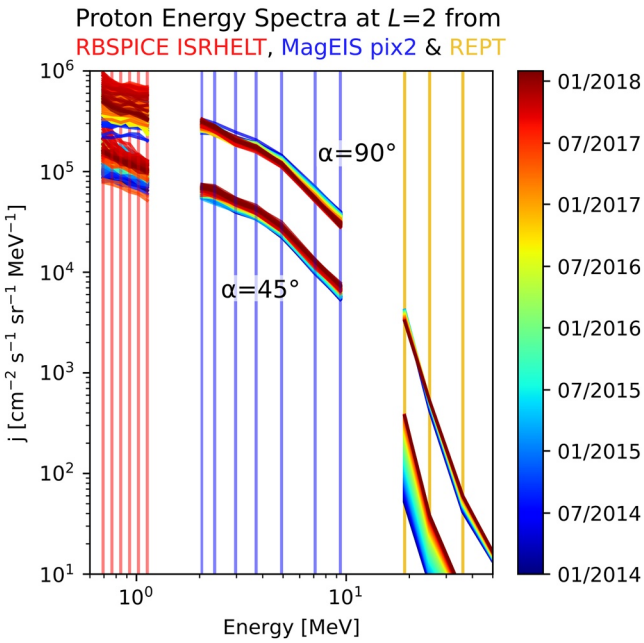

Figure 2. The proton energy spectrum at $L = 2$ derived from fitting a time series of pitch angle distributions to each energy channel. Energy channels are shown by vertical lines and correspond to three separate instruments: Radiation Belt Storm Probes Ion Composition Experiment (0.69–1.13 MeV, red); Magnetic Electron Ion Spectrometer (2.05–9.38 MeV, blue) and Relativistic Electron-Proton Telescope (REPT) (19–60 MeV, amber). The REPT data was derived approximately by fitting pitch angle distributions to the data in Figure 7 of Selesnick and Albert (2019).

data in panel a, the standard deviations in pix2 flux is low. This indicates that higher energies exhibit less variability over the same six day window. Figure 1, right side of panel b, also shows the ratio of the standard deviation to the absolute flux value in the 90° bin, taken from fits to the data at $L = 2$ over each time interval. The data shown for MagEIS pix2 at 4.92 MeV in Figure 1 is representative for all channels.

2.2.2. Data Issues and Validation

Using the 4.92 and 22.5 MeV pix2 data to calculate omnidirectional flux results in a strong correlation in values between the two channels at $L < 1.9$, indicating that data is highly contaminated in this region, presumably from energetic (100s MeV) inner belt proton contamination. In addition, there are periodic spikes in intensity in channels below ~4 MeV at $L > 3$, indicative of contamination by Bremsstrahlung in the presence of multi-MeV electrons. However, at $L = 2 \pm 0.02$, pitch angle distributions do not show obvious signs of contamination and have low intensity in the loss cone. At $L = 2$ below ~5 MeV, there is a reasonably close agreement (in general by a factor of ~2 or less) between this data and fluxes modeled using AP9 V1.50 mean (Ginet et al., 2013). At >10MeV, this data has worse agreement and, on the highest energy channel (22.5 MeV), directional flux at 90° pitch angle is much lower than recorded by the low energy channels on the REPT instrument. We therefore limit our use of MagEIS pix2 data to the seven energy channels covering 2.05–9.38 MeV at $L = 2$.

2.3. Energy Spectrum

After restricting the data as described above, flux was available at six energy channels from the RBSPICE ISRHELT product and seven channels from the MagEIS pix2 detector. Fitted equatorial pitch angle distributions were used to derive a time-varying energy spectrum at $L = 2$ across the ~four year modeling period, which could then be used as the outer model boundary in a numerical simulation. The spectrum is shown in Figure 2 for two values of equatorial pitch angle (45° and 90°), with the energy of each data channel indicated by vertical colored bars for each instrument. In addition to ISRHELT (red lines in Figure 2) and MagEIS pix2 (blue lines in Figure 2), proton data from the REPT instrument has been included to help constrain the spectrum at higher energies (amber lines in Figure 2). The inclusion of this data was approximate; we derived time-varying equatorial pitch angle distributions by digitizing the data shown in Figure 7 of Selesnick and Albert (2019). This figure shows unidirectional proton flux at $E \geq 19$ MeV for five epochs covering the modeling period derived from REPT measurements. Data is shown for equatorial pitch angles of 90° and 60°, and we used these two data points at $L = 2$ to derive the pitch angle distribution by assuming a distribution of the form $j = A\sin^n(\alpha_{eq})$ and solving for the two unknowns A and n. Extending the spectrum to higher energies was important because coulomb collisional loss leads to a convection of phase space density to lower values of μ, meaning that uncertainty at high energies affects lower energies too. However, we compared different spectrum fits at high energy to understand this sensitivity, and found that changes in the high energy ($\gtrsim$30 MeV) spectrum did not introduce significant changes at the $\lesssim$10 MeV energy range that is the focus of this study.

The color bar in Figure 2 shows how flux varies through time at the outer boundary of our modeling region. An interesting feature of the 90° spectrum is that over the intermediate energies (from ~2 until 20 MeV), flux starts high in 2014 (blue) and decreases toward the end of the modeling period in 2018 (red), but outside this energy range there is an increase in flux. In contrast, the data at 45° shows an increase in flux through time at all energies. These two trends indicate that, at intermediate energies where flux decreases at 90°, there is a steady reduction in anisotropy over the four year period leading to wider equatorial pitch angle distributions. Throughout the four year modeling period, there are times where boundary data is unavailable at certain energy channels, and this is indicated by the white unshaded regions in Figure 1. We dealt with this by simply interpolating from pitch angle distributions surrounding the data outage period, allowing a continuous spectrum.

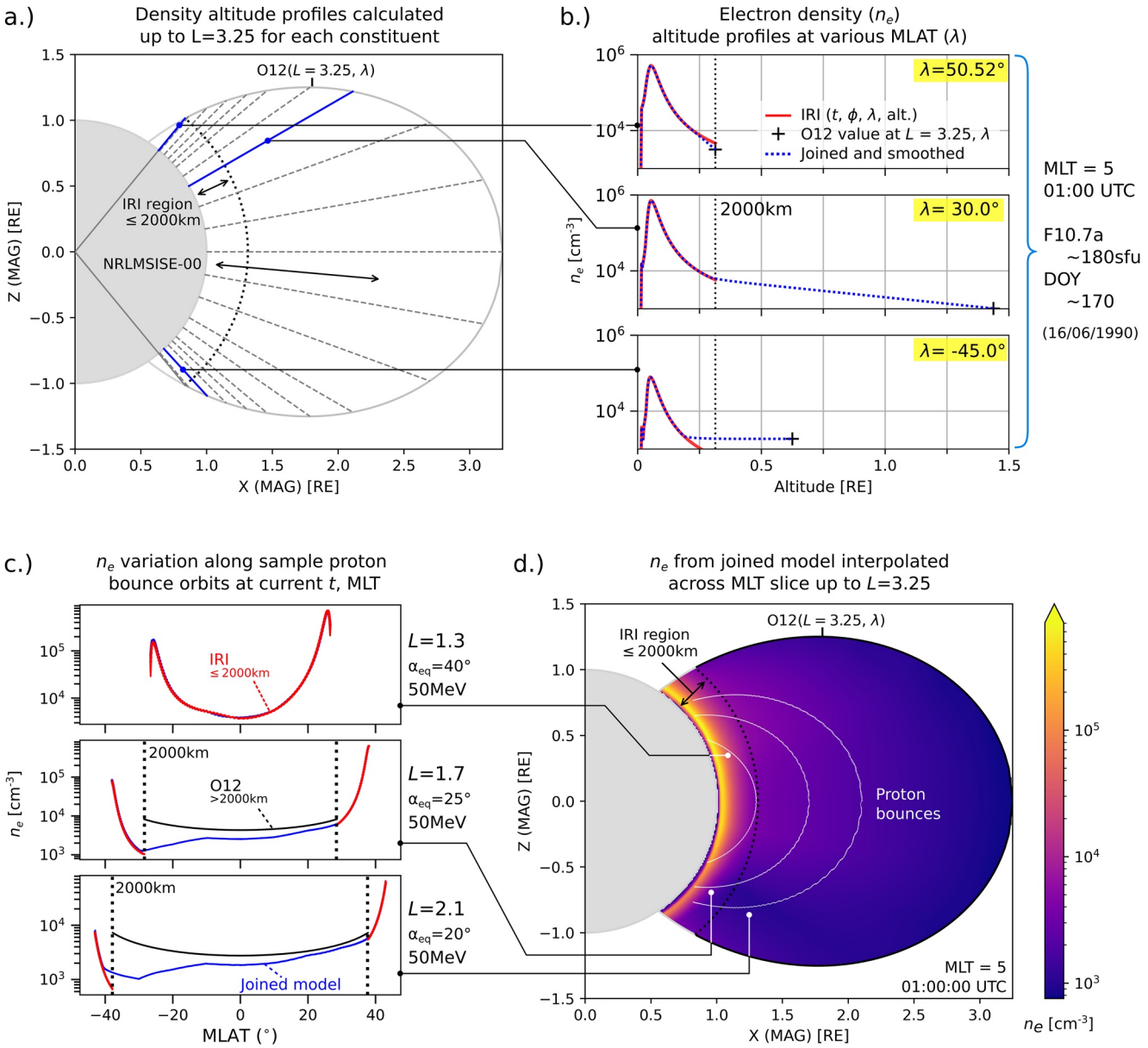

Figure 3. An overview of the construction of the BAS-PRO drift averaged density model (for the case of electron density). The top left panel shows density profiles calculated at regular intervals in magnetic latitude, derived by interpolating and smoothing between the values given by International Reference Ionosphere at ≤2000km and the O12 model at $L = 3.25$, as shown in the top right panel for three selected altitude profiles. The bottom right panel shows the result of interpolating between these altitude profiles of electron density across an magnetic local time (MLT) slice, and the bottom left panel shows the variation in electron density along three example proton bounce orbits at this MLT as a function of magnetic latitude (each bounce orbit is also drawn on the bottom right panel).

3. The BAS-PRO Model

3.1. Model Overview

The BAS-PRO model solves for relativistic phase space density as a function of the three adiabatic invariants μ, K and L. The following definitions are used for these quantities:

$$\mu = \frac{T(T + 2E_0)}{2E_0 B_m} \tag{3}$$

$$K = \sqrt{B_m} I \tag{4}$$

$$L = \frac{2\pi a^2 B_0}{\Phi} \tag{5}$$

where T is kinetic energy, E_0 is proton rest energy, B_m is the geomagnetic field strength at the mirror point along a bounce orbit, a is the radius of Earth, B_0 is the mean value of the equatorial geomagnetic field strength at Earth's surface, and Φ is the magnetic flux enclosed by a drift path. The geomagnetic field is modeled as a dipole, with $B_0 = 2.986\,7 \times 10^{-5} T$ (calculated for the year 2015 using coefficients of the IGRF magnetic field model, Alken et al., 2021). Additionally we make use of the following approximation for I:

$$I = \frac{1}{2}\oint \cos(\alpha_{eq}) ds \approx LaY(y) \tag{6}$$

where the integral takes place along a bounce path s, y is the sine of equatorial pitch angle, and Y is given by Equation 161 in Schulz (1991). The right hand side of this equation is an approximation for a dipole magnetic field.

Phase space density is given by j/p^2 with SI units of $m^{-6}s^3kg^{-3}$, where j is unidirectional differential proton flux and p is momentum. We model the quantity $f(\mu, K, L)$ given by $f = m_0^3 j/p^2$, where m_0 is the proton rest mass. This quantity is proportional to phase space density by a constant, but we find the units more convenient for comparison with other works. We numerically solve for f using an equation derived by expanding the Fokker-Planck equation in terms of three adiabatic invariants μ, J and L, where $J = 2pI$ is an alternative definition of the second invariant, and considering only the D_{LL} element of the diffusion tensor (see Beutier et al., 1995), leading to

$$\frac{\partial f}{\partial t} + \frac{\partial}{\partial \mu}\left[\left(\frac{\mathrm{d}\mu}{\mathrm{d}t}\right)_{fric} f\right] + \frac{\partial}{\partial J}\left[\frac{J}{2\mu}\left(\frac{\mathrm{d}\mu}{\mathrm{d}t}\right)_{fric} f\right] = L^2 \frac{\partial}{\partial L}\left[\frac{D_{LL}}{L^2}\frac{\partial f}{\partial L}\right] + S_n - \Lambda f \tag{7}$$

Equation 6 is used to define $J = 2pLaY(y)$, which leads to the result $\left(\frac{\mathrm{d}J}{\mathrm{d}t}\right)_{fric} = \frac{J}{2\mu}\left(\frac{\mathrm{d}\mu}{\mathrm{d}t}\right)_{fric}$ (Farley & Walt, 1971). Equation 7 has been simplified using this result, and contains extra terms describing the CRAND source (S_n) and loss from nuclear collisions and charge exchange (Λf). The quantity $\mathrm{d}\mu/\mathrm{d}t_{fric}$ represents the change in μ due to coulomb collisions, a cumulative effect of many small deflections by free and bound electrons in the atmosphere, ionosphere and plasmasphere. Substituting $B_m = B_e/\sin^2(\alpha_{eq})$ into Equation 3 and differentiating gives

$$\left(\frac{\mathrm{d}\mu}{\mathrm{d}t}\right)_{fric} = \left\langle \frac{\mathrm{d}T}{\mathrm{d}x} \right\rangle \frac{(T^2 + 2E_0T)^{\frac{1}{2}}}{B_e m_0 c} \sin^2(\alpha_{eq}) \tag{8}$$

where $\left\langle \frac{\mathrm{d}T}{\mathrm{d}x} \right\rangle$ is the mean kinetic energy loss averaged along a particle drift orbit. The quantity $\left\langle \frac{\mathrm{d}T}{\mathrm{d}x} \right\rangle$ has contributions due to drift averaged electron density $\langle n_e \rangle$ and gas molecule density $\langle n_i \rangle$, and is given in SI units by:

$$\begin{aligned}\left\langle \frac{\mathrm{d}T}{\mathrm{d}x} \right\rangle = \; & \frac{4\pi}{m_e v^2}\left(\frac{e^2}{4\pi\epsilon_0}\right)^2 \left(\langle n_e \rangle \left[\beta^2 - \ln(\lambda_D m_e v/\hbar)\right] + \right. \\ & \left. \sum_{n=1}^{N} \langle n_i \rangle Z_i \left[\beta^2 - \ln((\gamma^2 - 1)2m_e c^2/I_i)\right]\right)\end{aligned} \tag{9}$$

where e is electron charge, Z_i is the number of bound electrons for each constituent, I_i is the mean excitation energy for bound electrons and λ_D is the drift average debye length (Schulz & Lanzerotti, 1974).

Four boundary conditions are applied to the model: (a) $f(\mu, K, L_{\min}) = 0$ where $L_{\min} = 1.15$, (b) $f(\mu_{\max}, K, L) = 0$ where $\mu_{\max} = 5000$ MeV/G (~170 MeV at $L = 2$), (c)$f(\mu, K_{lc}, L) = 0$ where $K_{lc}(L)$ is the lowest K on the model grid that is inside the loss cone at L, and (d) $f(\mu, K, L_{\max}, t) = f_b(\mu, K, t)$ where $L_{\max} = 2.0$ and $f_b(\mu, K, t)$ is the time-varying outer boundary spectrum specified from the Van Allen Probe measurements and extrapolated across the range in μ.

A close fit to the spectrum data is achieved by making f_b a combination of two polynomial fitting functions P_1 and P_2, which are re-derived for every value of K on the boundary to fit the curve of log $j(E, \alpha_{eq})$ versus energy. This curve is calculated by taking the logarithm of the data shown in Figure 2. P_1 is a first order polynomial (straight line fit) derived to fit data points log $j(E \leq 7$ MeV), and P_2 is a second order polynomial derived to fit data points log $j(E \geq 5$ MeV). The gradient $\mathrm{d}P_2/\mathrm{d}E$ at the highest energy channel is used to linearly extrapolate

log j to higher energies outside the data range, thereby transitioning P_2 into a straight line fit. f_b (in terms of flux) is then given according to:

$$f_b = \begin{cases} e^{P_1}; E \leq 5\text{MeV} \\ Ae^{P_1} + Be^{P_2}; 5 < E < 7\text{MeV} \\ e^{P_2}; E \geq 7\text{MeV} \end{cases} \quad (10)$$

where A and B vary linearly with energy from $A = 1, B = 0$ at 5 MeV to $A = 0, B = 1$ at 7 MeV so that f_b is linearly interpolated in this range from the two fitting functions.

3.2. Modeling Loss

3.2.1. Coulomb Collisions

Coulomb collisions with free and bound electrons in the plasmasphere, ionosphere and atmosphere cause energy loss which results in the convective flow of f to lower μ. Changes in f are controlled in Equation 7 by the μ degradation term $d\mu/dt_{fric}$, as well as the local spectrum $\partial f/\partial\mu$.

The drift averaged densities $\langle n_i \rangle$ and $\langle n_e \rangle$ are required to evaluate $d\mu/dt_{fric}$ via Equations 8 and 9. We composed a model to calculate drift averaged density throughout the region of interest, using a combination of three existing density models: NRLMSIS-00 (Picone et al., 2002), the International Reference Ionosphere (IRI, Bilitza et al., 2017) and the plasmasphere model of Ozhogin et al. (2012) (from hereon referred to as "O12"). Section 3.2.3 details this method. The new drift averaged density model preserves seasonal and solar cycle variations exhibited by the NRLMSIS-00 and IRI models, and provides drift averaged density for 14 constituents as a function of F10.7a (81 day average solar radio flux), day of the year (DOY), and drift orbit coordinates μ, K and L.

These changes in density drive time variability in $d\mu/dt_{fric}$ at a given set of model coordinates. The energy and pitch angle dependence of $d\mu/dt_{fric}$ also leads to significant variations in the loss rates at different coordinates. This variation is analyzed in Section 3.2.4.

3.2.2. Nuclear Scattering

In addition to coulomb collisions, radiation belt protons are lost due to inelastic nuclear scattering, although this type of loss operates on longer timescales (Albert et al., 1998). The effect of inelastic nuclear scattering against the nuclei of various atmospheric constituents is taken into account via the loss term Λ in Equation 7. For a proton at velocity v,

$$\Lambda = v \sum_i \sigma_i \langle n_i \rangle \quad (11)$$

where $\langle n_i \rangle$ is the drift averaged density of constituent i, and σ_i is the scattering cross section for a collision between a proton at velocity v and a nuclei of constituent i. The summation is evaluated over i = H, He, N, O and Ar. For Hydrogen, σ_H is the total combined cross section for elastic and inelastic interactions from Figure 1 of Meyer (1972), whilst other σ_i are the cross sections for inelastic collisions calculated using the empirical formula given by Letaw et al. (1983).

As in the case of $d\mu/dt_{fric}$, Equation 7 was evaluated using $\langle n_i \rangle$ given by the drift averaged density model, and Λ also undergoes time variability at each adiabatic coordinate. The inelastic nuclear scattering process is also a source term at lower energy, since protons are re-distributed in phase space but may still be trapped (Selesnick et al., 2007). However, we assume this source process to be negligible.

3.2.3. Drift Averaged Density

The first step toward calculating the drift averaged density model was solving a range of proton drift orbit trajectories covering the modeling domain. Protons were initialized at coordinates of μ, α_{eq} and L covering the

range $\sim 1 \leq \mu \leq 10\,000$ MeV/G at a spacing of $\Delta \log_{10}\mu \sim 0.09$, and $1.1 \leq L \leq 3.5$ at a spacing of $\Delta L = 0.02$, with equatorial pitch angles at 1° intervals ranging from inside the loss cone to $\alpha_{eq} = 90°$. Drift trajectories were calculated by solving the relativistic equation of motion for a magnetic dipole field (using the same value of B_0 as the model for 2015).

To calculate drift averaged density, we must first be able to determine the density of each constituent at every point along each solved proton trajectory in our region of interest. Neutral density of He, O, N2, O2, Ar, H, N and anomalous O is given by NRLMSIS-00 below 2000 km. To calculate it above this height, we extrapolate it as a straight line of $\log10(n_i)$ with altitude. Ion density of O+, H+, He+, O2+, and NO+ is given by IRI below 2000 km and is extrapolated to higher altitudes via the same method. Electron density is also given by IRI below 2000 km, and above 2000 km is interpolated between IRI and the O12 model value at $L = 3.25$. The latter is based on a fit to Radio Plasma Imager data from the IMAGE satellite (Ozhogin et al., 2012) and is a static value, unlike the IRI and NRLMSIS-00 models which include various dependences. However, historical measurements indicate relatively consistent electron density at $L = 3.25$ below the plasmapause (see for example Figure 10, Park et al., 1978), and there is a good agreement between empirical models here too (Ozhogin et al., 2012). Smoothing of the electron density profile with altitude is performed to ensure a physical profile. This is achieved by defining a transition region near 2000 km and using Bézier curves to connect the electron density profile from IRI to the static value of Ozhogin et al. (2012). Panels a and b of Figure 3 illustrate this process. Panel a shows altitude profiles constructed at regular intervals in magnetic latitude. Along each of these profiles, neutral, ion and electron density is returned from the models as specified above. Panel b shows an example of electron density along three altitude profiles at different magnetic latitudes. The dashed blue line in each of these profiles represents the final electron density profile as a result of smoothing the values between IRI (shown in red) and O12 at $L = 3.25$ (black + symbol). These values correspond to the coordinates indicated on the right of the top right panel in Figure 3.

Density is next interpolated between the altitude profiles across magnetic latitude to construct a density slice in the meridian plane at a given magnetic local time (MLT). This is demonstrated for electron density at an example MLT in panel d of Figure 3, using the density values from the profiles shown in panels a and b. It is important to note that electron density shown in panel d is calculated for a specific time of day, MLT, F10.7a and DOY.

To achieve the solar cycle and seasonal dependence of our drift average density model, five different values of F10.7a were considered (60, 100, 140, 180, 220 solar flux units, sfu) along with four days of the year (DOY; day 70, 170, 270, 330). Twenty past environments matching each possible combination of F10.7a, DOY were found by searching through a time history of indices. Once a date had been found with a F10.7a, DOY coordinate matching each combination (within a margin of ±10 sfu, ±4 days), density of each constituent was drift averaged by querying each model in the fashion described above using the time corresponding to that F10.7a, DOY coordinate as model input. To eliminate day-night variation in density, each drift average was performed six times (at four hour intervals) throughout the day selected. MLT variation is automatically accounted for by considering the particle trajectory around Earth. The density returned by the NRLMSIS-00 and IRI models for a test point occasionally showed large time-dependent changes appearing to correlate with jumps in daily AP index. This variability was excluded from the above drift averages by manually checking that each of the 20 environments corresponded to magnetically quiet conditions with daily AP < 12.

To show how the drift averaged density values were derived, and why smoothing of electron density was necessary, Figure 3, panel c, shows the variation of electron density versus magnetic latitude along three proton bounce orbits, derived using density at the MLT shown in panel d. The energy, equatorial pitch angle and L of the proton bounce is labeled next to each profile, and each orbit is also drawn onto the MLT slice in panel d. Density returned directly from the IRI model is shown in red up to 2000 km, the maximum height of the model. Likewise, density returned directly from the O12 model is shown in black above 2000 km, which is the minimum height of the model. The second and third bounce orbits in panel c cross 2000 km, and for these two orbits Figure 3 shows the mismatch in electron density at 2000 km (red vs. black) according to IRI and O12. The discrepancy would introduce steep gradients into the drift averaging results if not smoothed, and depends on MLT, time, etc. In contrast, the blue line in each profile represents the smoothed electron density derived by combining IRI values up to 2000 km and O12 values at $L = 3.25$. Each bounce orbit mirrors at low altitude close to the loss cone, and therefore density is high at the mirror points as each proton penetrates the atmosphere.

3.2.4. Variation in Loss Rates

The drift averaged density model was used to calculate $\left\langle \frac{dT}{dx} \right\rangle$ in Equation 9 and Λ in Equation 11 by resolving the unknowns $\langle n_e \rangle$ and $\langle n_i \rangle$. The Debye length term in Equation 9 was calculated using the drift averaged ion and electron temperatures $\langle T_i \rangle$ and $\langle T_e \rangle$, which were calculated alongside the drift averaged densities using IRI. As a result of the drift averaging method, there are 20 sets of $\langle n_e \rangle$, $\langle n_i \rangle$, $\langle T_i \rangle$ and $\langle T_e \rangle$ values, corresponding to the set of drift averages calculated at five values of F10.7a, and on four different days of the year. Therefore, $\left\langle \frac{dT}{dx} \right\rangle$ is a function of particle coordinate μ, K and L, as well as F10.7a and DOY. The $\left\langle \frac{dT}{dx} \right\rangle$ term was used to calculate $d\mu/dt_{fric}$, which is also therefore a function of the particle coordinate, F10.7a and DOY.

To demonstrate these results, characteristic timescales of coulomb collisional loss and inelastic nuclear scattering have been calculated at two different epochs over the modeling period, and are plotted in Figure 4 for proton energies 1, 10 and 35 MeV (first, second and third rows respectively). The timescale for coulomb collisional loss was approximated as $\tau_{cc} = (d\mu/dt_{fric})/\mu$, and the timescale for inelastic nuclear scattering was given by Λ. The left hand column of Figure 4 shows loss timescales for particles with $\alpha_{eq} = 90°$ calculated for 18 June 2017. This corresponds to an epoch where F10.7a = 75.7sfu and DOY = 170, and so each value of $d\mu/dt_{fric}$ and Λ has been interpolated at these conditions from pre-calculated values at each of the 20 F10.7a, DOY drift average coordinates. The timescale τ_{cc} has been split into three components, representing the individual contributions from coulomb collisions with atmospheric neutral constituents (blue), ionospheric constituents excluding electrons (amber), and electrons throughout the ionosphere and plasmasphere (red).

For comparison, the central column of Figure 4 shows loss timescales for equatorially mirroring particles calculated for 27 November 2014, when F10.7a peaked during the simulation near solar maximum with a value of 162.4sfu. The right hand column of Figure 4 also shows loss timescales on 27 November 2014, but for particles with $\alpha_{eq} = 50°$, mirroring at latitudes away from the equator. The gray shaded region in the right hand column indicates coordinates in the loss cone.

Figure 4 shows that coulomb collisions are the dominant loss process for all energies under investigation, and that loss due to inelastic nuclear collisions (light blue curve) has a relatively small impact. In particular, coulomb collisions with free electrons in the plasmasphere (red curve) are dominant at $L \sim 2$, whilst coulomb collisions with neutral constituents (blue curve) become dominant at some lower L that depends on solar cycle and season. Comparing the left and central columns for a given energy also shows that during the transition from solar maximum (central column) toward solar minimum (left column), the loss timescale for coulomb collisions with the neutral atmosphere falls to around half its prior value at $L \lesssim 1.2$, but is relatively unaffected at $L = 1.4$. This is due to cooling and shrinking of the atmosphere.

Figure 4 illustrates two more important features of coulomb collisional loss timescales. The first is seen by comparing τ_{cc} in the central column and right hand column: protons mirroring at higher latitudes experience a higher rate of loss compared with equatorially mirroring protons of the same energy and L. This is a density-driven effect, because particles mirroring at higher latitude pass through denser regions of the atmosphere at lower altitude. The second feature is seen by comparing τ_{cc} in the top, middle and bottom rows of a given column: lower energy protons are subject to higher loss. This is not a density driven phenomenon, it occurs due to the energy dependence of Equation 8. Li et al. (2020) show the variation in 36 MeV integral flux driven by solar cycle density variation, and note how this effect becomes very weak at $L > 1.2$. However a comparison between the top and bottom rows in Figure 4 shows that 1 MeV particles are subject to significantly higher loss rates than at 35 MeV. This implies that lower energy particles are also more sensitive to solar cycle variations in density, and therefore solar cycle variations in density may drive variability at $L > 1.2$ in flux at some energies below 36 MeV.

3.3. Diffusion Coefficients

We define D_{LL} in Equation 7 according to empirically-derived expressions used in previous literature. There are considerable differences between both the magnitude of D_{LL} and its dependencies between works, reflecting different applications. Three sets of D_{LL} were chosen to demonstrate this range. Each is presented in this section, then used to produce simulation results for comparison.

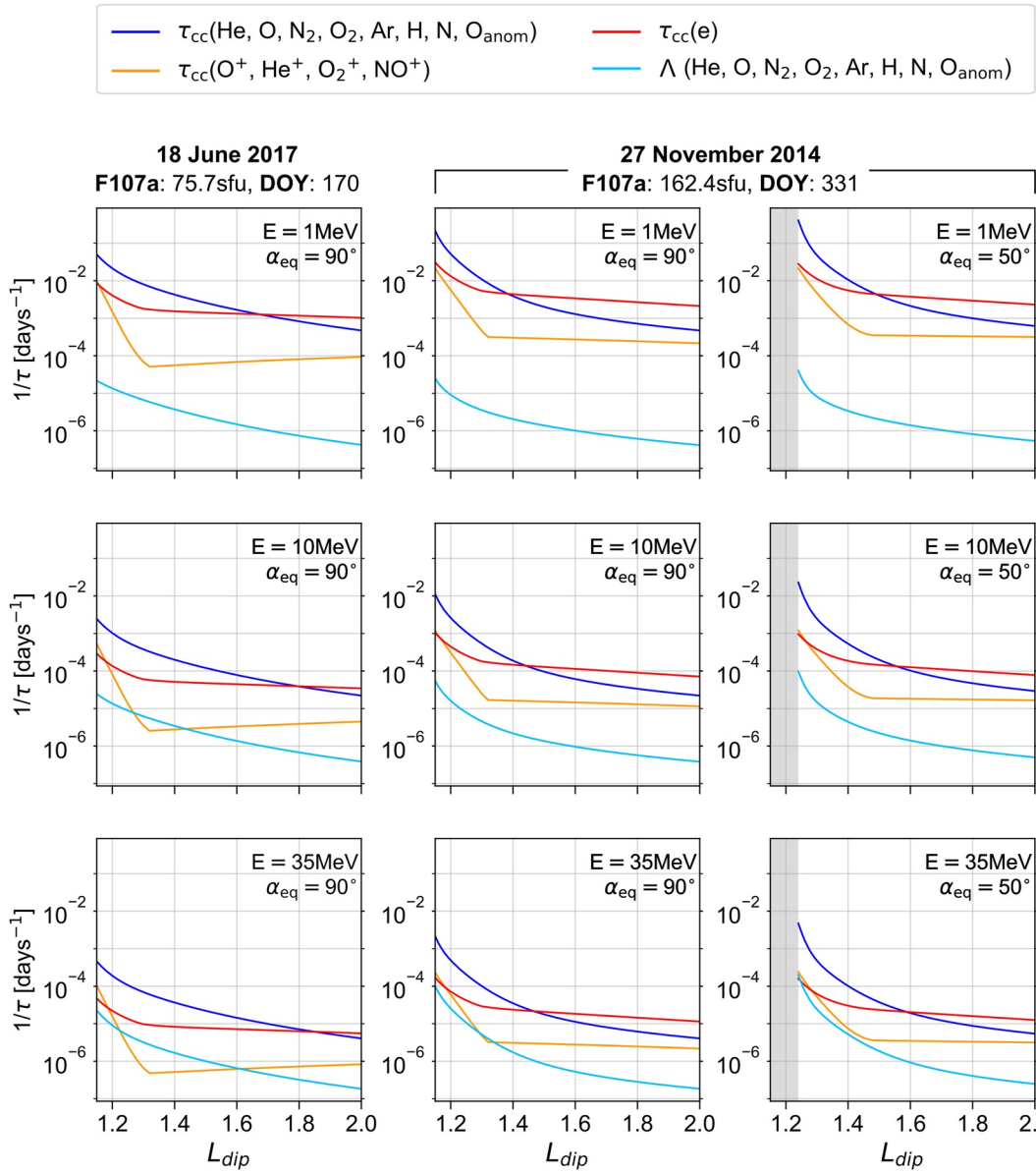

Figure 4. Timescales for coulomb collisional loss τ_{cc} and inelastic nuclear scattering Λ are shown as a function of energy (rows) and for two different epochs (left column vs. center and right column). Left and center columns plot loss timescales for equatorially mirroring protons, whilst the right column shows loss timescales for particles with equatorial pitch angle $\alpha_{eq} = 50°$. The timescale for coulomb collisional loss has been separated into three components (blue, amber and red), corresponding to the contribution from each group of constituents indicated by the legend (top of figure).

The first equation for D_{LL} is from Equation 5 of Selesnick and Albert (2019). In the original work it is applied to model high energies ($\geq$ 19MeV) after 1 January 2015. It is modified slightly here, with the $y = 1 - K/(0.58\ \mathrm{G}^{1/2}\mathrm{R}_E)$ term in the original work being replaced by $\sin(\alpha_{eq})$:

$$D_{LL}(\alpha_{eq}, L) = 1.4 \times 10^{-13} L^{10} \sin^{1.6}(\alpha_{eq}) \mathrm{s}^{-1} \tag{12}$$

The second D_{LL} represents the magnetic diffusion coefficient required to produce a good comparison with experimental data at $E > 10$ MeV by Jentsch (1981). It was also used by Selesnick et al. (2007):

$$D_{LL}(E, \alpha_{eq}, L) = 3.75 \times 10^{-12} L^{9} \left(\frac{1\mathrm{MeV}}{E}\right) \sin^{2.7}(\alpha_{eq}) \mathrm{s}^{-1} \tag{13}$$

The third D_{LL} is the same as Equation 12 of Selesnick et al. (2016) except for the dipole dependence term, which we assume here is equal to 1 because we consider Earth's dipole as fixed over the modeling period. This D_{LL} was originally used to produce a fit with REPT data at $E \geq 24$ MeV.

$$D_{LL}(E, L) = 6 \times 10^{-11} L^9 \left(\frac{1\text{MeV}}{E} \right)^{3/2} \text{s}^{-1} \tag{14}$$

The three sets of D_{LL} are each used to calculate $f(\mu, K, L)$ whilst keeping all other model parameters constant. We refer to the three corresponding model runs as "SA19", "J81" and "S16" respectively, based on abbreviations of the works from which each D_{LL} was taken. In these original works, each D_{LL} value was found to produce agreement between measured and computed values. However, compared to the original works, we are applying these values to model lower energy protons. This has a varying effect on the value of each D_{LL}, as the D_{LL} of Selesnick and Albert (2019) does not include energy dependence, whereas the other D_{LL} do, with the energy dependence of D_{LL} from Selesnick et al. (2016) being strongest.

3.4. CRAND

CRAND is the primary source of protons at $\gtrsim$50 MeV at low L (Selesnick et al., 2007), occurring when interactions between the atmosphere and incoming galactic cosmic rays produce an upward-moving neutron, which undergoes beta decay to a proton and electron (and an antineutrino). The proton and electron then become trapped (e.g., Li et al., 2017; Singer, 1958). Following the definition $f = m_0^3 j / p^2$, the rate of change in model phase space density due to CRAND is given by

$$S_n = \frac{\partial}{\partial t} \left(m_0^3 \frac{j_p}{p^2} \right) = \frac{m_0^3}{p^2} \left(\frac{\partial j_p}{\partial t} \right) \tag{15}$$

where $\partial j_p / \partial t$ is the rate of change in proton flux at a set of adiabatic coordinates caused by the pickup of newly produced protons. As the set of adiabatic coordinates corresponds to a drift orbit, $\partial j_p / \partial t$ is given by

$$\frac{\partial j_p}{\partial t}_{n} = \frac{\oint_S \boldsymbol{j_n} \cdot \mathrm{d}\mathbf{s}}{\gamma \tau_n \oint_S \mathrm{d}s} = \frac{\langle j_n \rangle}{\gamma \tau_n} \tag{16}$$

where the integral takes place along a proton drift orbit S, d$\mathbf{s}$ is an element of length along the trajectory, $\boldsymbol{j_n} \cdot \hat{\mathbf{ds}}$ is the flux of neutrons leaving the atmosphere in a direction coinciding with the section of drift orbit, and $\gamma \tau_n$ is the relativistic neutron lifetime where $\tau_n = 887$s (Dragt et al., 1966; Selesnick et al., 2007). For each position along S, neutron flux $\boldsymbol{j_n}$ is determined at the point on top of Earth's atmosphere that is intersected by following the negative tangent to S in the $-\hat{\mathbf{ds}}$ direction. For positions where there is no such intersection, $j_n = 0$. The quantity $\langle j_n \rangle$ therefore represents average atmospheric neutron albedo flux in the direction of a proton along its drift. Equation 16 assumes that the proton produced moves in the same direction of the decaying neutron (Selesnick et al., 2007) and absorbs all its kinetic energy.

To find $\boldsymbol{j_n}$ at an atmospheric intersection point, we use data computed for the previous work of Selesnick et al. (2007) which specifies directional neutron albedo flux at the top of the atmosphere. This data is the result of modeling the interactions of incoming galactic cosmic rays throughout the atmosphere, and gives $j_n = j_n(E_n, \text{z}, \mathcal{R}_{cv}, \text{F10.7})$, where E_n is kinetic energy, z is zenith angle and $\mathcal{R}_{cv}$ is vertical geomagnetic cutoff rigidity. A latitudinal dependence of j_n arises via $\mathcal{R}_{cv}$, and solar cycle dependence via F10.7. Zenith angle is found by considering the direction $\hat{\mathbf{ds}}$ relative to a coordinate system local to the atmospheric intersection point, with an upwards-pointing vertical axis defining the direction of zero zenith. Equation 4 of Smart and Shea (2005) gives geomagnetic cutoff rigidity as a function of zenith angle and latitude using mixed CGS units. We adapt this equation to find vertical geomagnetic cutoff rigidity $\mathcal{R}_{cv}$ (zenith equal to zero) in SI units, giving

$$\mathcal{R}_{cv} = \frac{\mu_E \cos^4(\lambda)}{4d^2(100a)^2} \quad \frac{3 \times 10^5}{1 \times 10^9} \tag{17}$$

where $\mathcal{R}_{cv}$ has units GV, μ_E is Earth's dipole moment (Am^2), d is distance from the dipole center in Earth radii, λ is magnetic latitude, a is Earth's radius (m), and the various other factors arise from the non-SI to SI conversion (see Smart & Shea, 2005).

The integral in Equation 16 was performed numerically to evaluate $\langle j_n \rangle$ across a set of proton drift orbit trajectories, with a detailed description of the steps included in Lozinski et al. (2021). For each drift orbit trajectory, $\langle j_n \rangle$ was computed for five values of F10.7 (60, 100, 140, 180, and 220 sfu), allowing the solar cycle dependence of S_n to be taken into account. The top of the atmosphere was approximated using the WGS84 ellipsoid (Decker, 1986) with an extra 100 km radius, tilted with respect to the dipole axis. Calculations of S_n extend from 2.31 MeV (the minimum energy for which neutron albedo data is available) up to 500 MeV. We then further extend the CRAND source below 2.31 MeV by linearly extrapolating the gradients in S_n with respect to energy at each model L and K, then smoothing the extrapolated data to produce approximate values covering the range of low energy coordinates.

As a test, we set $S_n = 0$ everywhere and calculated steady state, then compared with results formed by non-zero S_n. This comparison showed that CRAND is important for forming the distribution even at a few MeV at $L < 1.3$. However this is mainly because phase space density is flowed to these coordinates from higher energy where S_n provides a source comparable to radial diffusion. More tests showed that extrapolating below 2.31 MeV as described had a negligible effect on the ~1 MeV distribution since S_n is very small at this energy, but this was done anyway to avoid discontinuities in the model.

4. Modeling Variability

4.1. Method

The BAS-PRO model was used to solve for $f(\mu, K, L)$ over the period from 1 January 2014 to 1 March 2018, using the outer boundary spectrum shown in Figure 2. Simulations of the model period were performed for the three sets of D_{LL} in Equations 12–14, with results denoted "SA19", "J81" and "S16' respectively. Prior to this, the initial condition for each model run was formed by computing the steady state solution at the model start time (1 January 2014). Each steady state solution was also calculated using the D_{LL} values corresponding to the dynamic simulation.

In addition to D_{LL}, the initial state of the proton belt was an uncertain aspect of the simulation. The proton belt is unlikely to be in steady state at any time due to the long timescales required by radial diffusion to rebalance changes in boundary flux that have been observed to occur at $L \geq 2$ on much shorter timescales (see for example, Figure 1, Selesnick et al., 2016). In previous work, we solved for equatorial steady state phase space density during the CRRES satellite era and found a particularly high deviation from steady state at $\mu \gtrsim 400$ MeV/G. More rigorous methods of initializing the proton belt, such as in Selesnick et al. (2007), require integrating changes in phase space density over a time history of SEP injections, geomagnetic secular variations, and other causes of long term variation. Regardless, such methods still depend on knowledge of the diffusion coefficients, which are poorly constrained at the energies we investigate. Therefore, we are somewhat limited by the current capabilities of our model, but the method of initializing the proton belt in steady state in a sense goes further to demonstrate the consequences of uncertainty in D_{LL}, which may lead to uncertain initialization either way.

Although the model is numerically implicit, it was found that numerical instabilities could be caused by large gradients in $d\mu/dt_{fric}$ across the model grid (Equation 8). Such instabilities can be avoided in two ways: reducing the timestep; or increasing the effective loss cone altitude. The latter approach works because large gradients tend to occur near the loss cone where gradients in atmospheric density are the highest. Therefore, a steady state solution was initially computed using a high altitude loss cone with a large timestep. A new simulation was then initialized using the previous solution but decreasing the loss cone altitude, requiring a reduced timestep for stability but less time to reach steady state. This process was repeated, with the final resolution corresponding to a dipole loss cone altitude of 585 km, where the boundary condition specifies that $f = 0$ at the equivalent value of K. This is somewhat higher than the ~300 km loss cone altitude predicted in Table 1 of Fischer et al. (1977), but was found to provide a good balance between the required run time and solution detail. Results of the three runs SA19, J81 and S16 are presented in the next section using this loss cone altitude.

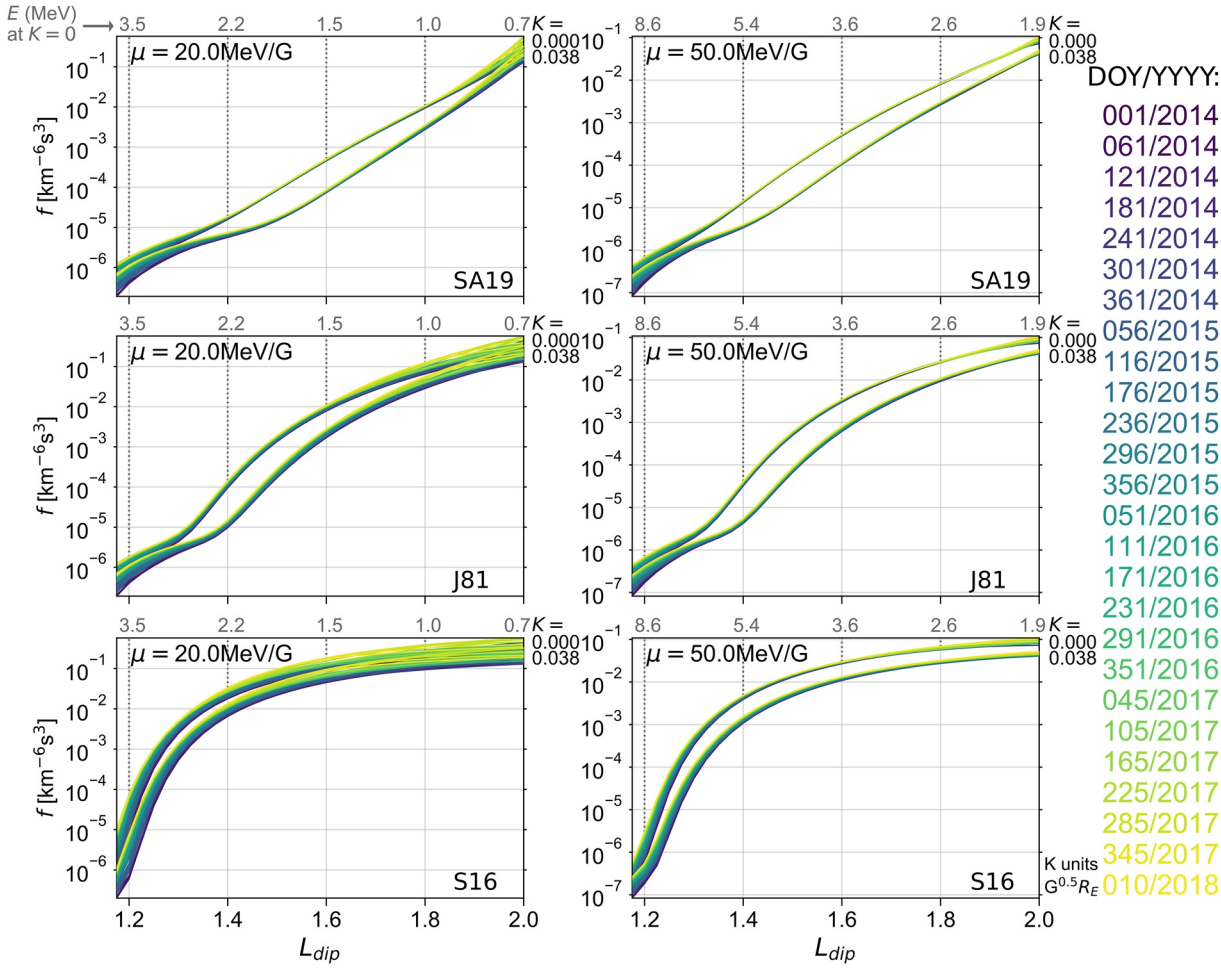

Figure 5. Solutions for relativistic phase space density $f = m_0^3 j/p^2$ at 30 day intervals over the modeling period, with colors corresponding to the dates shown on the right hand side. The column on the left shows f at a fixed value of $\mu = 20$ MeV/G, with $\mu = 50$ MeV/G solutions shown on the right. Each row corresponds to a different model run, characterized by the different sets of D_{LL} used (labeled within each panel).

4.2. Results

Figure 5 shows the radial profile of phase space density f over the modeling period at fixed values of $\mu = 20$ MeV/G and $\mu = 50$ MeV/G (left and right columns respectively), repeated for each of the three model runs (rows one to three show SA19, J81 and S16 respectively). The solution is shown for two values of the second invariant K, with $K = 0$ representing equatorial particles. Energy $E(\mu, K, L)$ corresponding to the values of μ on the horizontal axis for $K = 0$ is labeled at the top of each plot in gray.

The value of D_{LL} increases in the model runs from SA19 to J81 to S16. Figure 5 shows that as a result, the phase space density f increases by up to three orders of magnitude at $L \sim 1.4$ for $\mu = 20$ MeV/G. At $L \sim 1.2$ for $\mu = 20$ MeV/G, f is very similar between the SA19 and J81 runs, and around one and a half orders of magnitude higher for S16. At $\mu = 50$ MeV/G, the increase in f at $L \sim 1.4$ from SA19 to J81 to S16 is still significant (around two orders of magnitude) but not as large as at $\mu = 20$ MeV/G. This indicates an increasing divergence in simulation results at lower energy, as each set of D_{LL} is extrapolated further away from the energy range it was originally derived to model. These large variations between model runs are primarily caused by differences in the steady state initial condition of each simulation. However, the differences in D_{LL} between runs also affects the region of time variability, with phase space density at $L \sim 1.5$ staying relatively constant over the four years during the SA19 run, but increasing by a factor of ~2 at 20 MeV/G in the S16 run.

Figures 6 and 7 show the evolution of pitch angle distributions during the J81 and S16 model runs respectively at selected L (increasing in columns left to right), and at selected fixed energies (increasing in rows top to bottom).

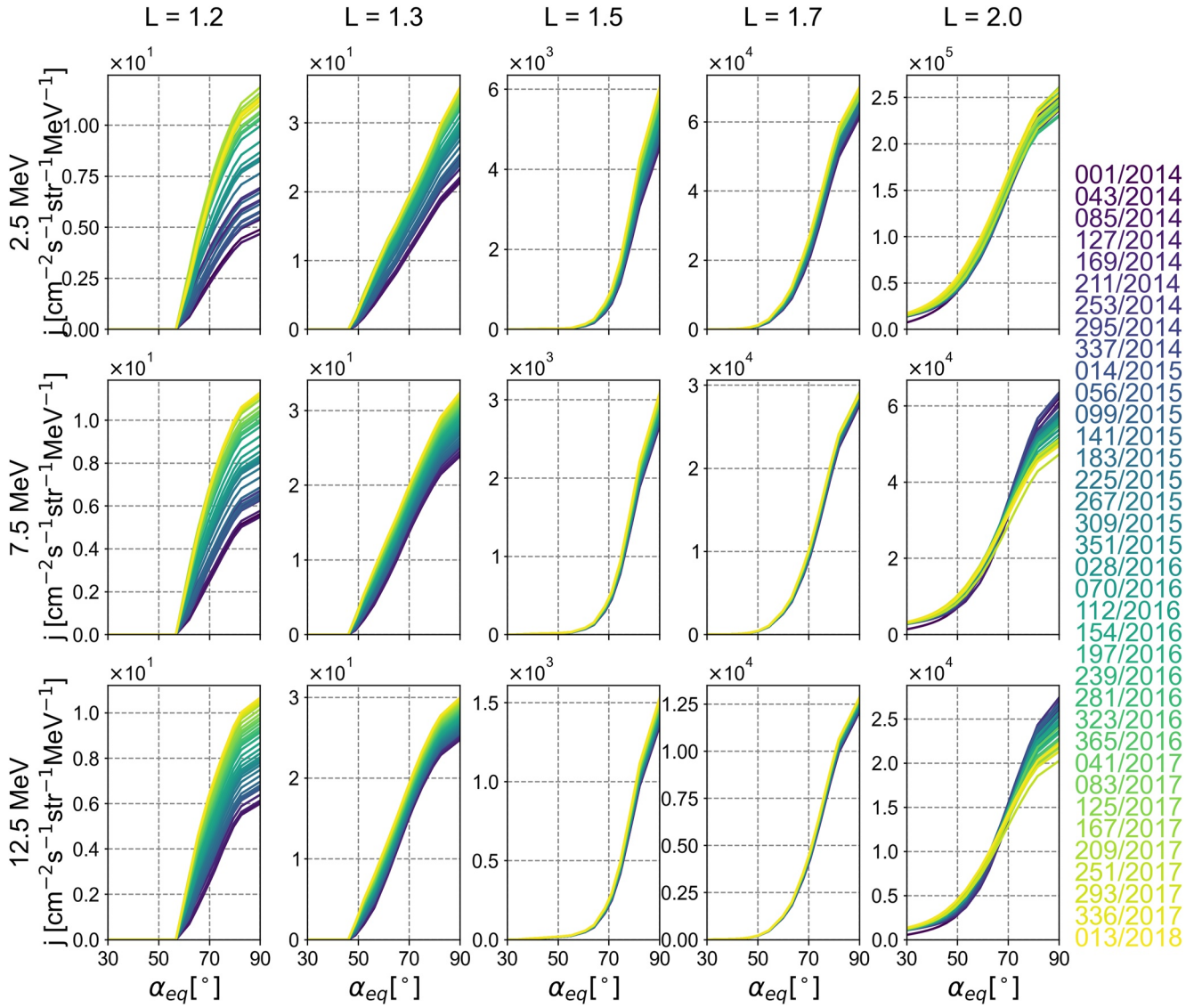

Figure 6. Solutions for equatorial pitch angle distributions of flux at fixed energies (rows) and L (columns) at 30 day intervals over the modeling period, with colors corresponding to the dates shown on the right hand side. These solutions were calculated for the J81 set of D_{LL}.

Figures 6 and 7 are plotted in terms of unidirectional flux at each energy rather than phase space density. The evolution of pitch angle distributions during the SA19 model run is not shown because the results are somewhat similar to the J81 results, with the main difference demonstrated by Figure 5: at $L \sim 1.5$, flux is over an order of magnitude lower than the J81 result, and shows less time variation.

Figures 6 and 7 highlight time variability during both the J81 and S16 model runs as opposed to changes between model runs caused by different initial conditions. One striking feature of both figures is the time evolution of distributions at $L = 1.2$. For example, at 2.5 MeV and $L = 1.2$ (top left panels), 90° flux approximately doubles over the modeling period during the J81 model run (Figure 6), and increases by nearly tenfold during the S16 model run (Figure 7).

Loss cone flux is fixed at zero, so the increases in 90° flux at $L = 1.2$ shown in Figures 6 and 7 give the impression of sharpening distributions through time. However, flux also increases at lower pitch angles such that the ratio of 90° flux to ~70° flux does not change much, and so anisotropy (as defined by the n parameter for a fit like $j \propto \sin^n \alpha_{eq}$) is relatively stable at a fixed L and energy during both model runs. To demonstrate this, Figure 8 plots

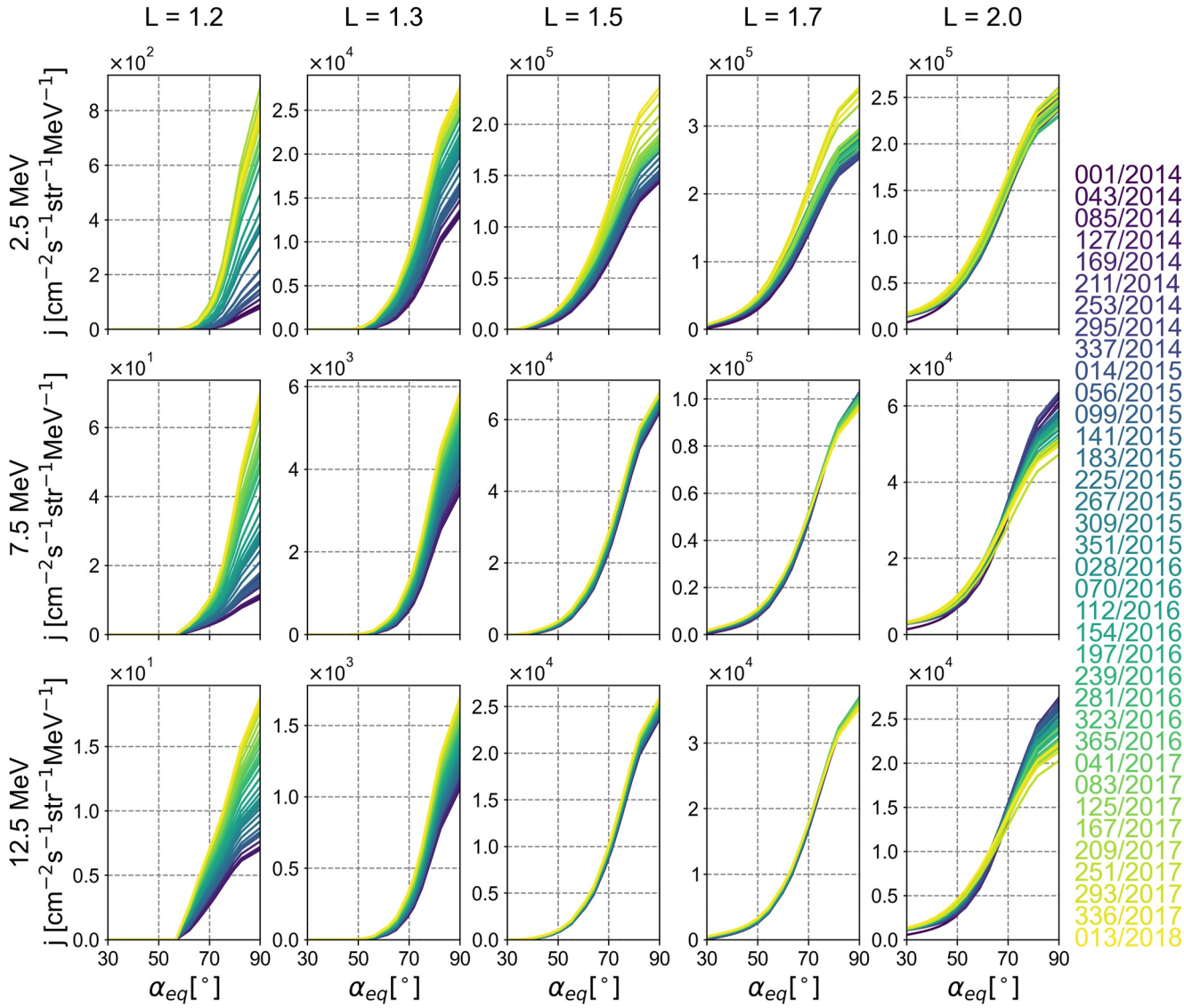

Figure 7. Solutions for equatorial pitch angle distributions of flux at fixed energies (rows) and L (columns) at 30 day intervals over the modeling period, with colors corresponding to the dates shown on the right hand side. These solutions were calculated for the S16 set of D_{LL}.

the anisotropy n versus L at the start and end time of each model run (solid blue and red curves respectively). The anisotropy is shown for energies 1, 10 and 45 MeV (left, center and right columns respectively).

Figure 8 shows that the largest change in anisotropy over time was during the S16 model run at $L = 1.2$ and ~1 MeV (solid curves in the bottom left panel): n decreases from ~55 to ~40. However, comparison of n between the SA19, J81 and S16 runs suggests that changes in anisotropy with L and energy are sensitive to the choice of diffusion coefficients. A key difference between each model run is the pitch angle and energy-dependence of D_{LL}. For example, in the J81 run $D_{LL}(E, \alpha_{eq}, L)$ decreases toward lower pitch angle, but in the S16 run $D_{LL}(E, L)$ is independent of pitch angle.

In order to better understand the dependence of anisotropy on D_{LL}, four extra model runs were performed. Two of these were variations of the SA19 and J81 model runs, in which pitch angle dependence of the original diffusion coefficients was eliminated. This was done by setting $\alpha_{eq} = 90°$ in Equations 12 and 13 for variations in each D_{LL} respectively. The other two runs were variations of the J81 and S16 model runs, in which energy dependence of the original diffusion coefficients was eliminated. This was done by fixing $E = 10$ MeV in Equations 13 and 14, to derive each new D_{LL} respectively. The anisotropy n of each of these four extra model runs is plotted in Figure 8

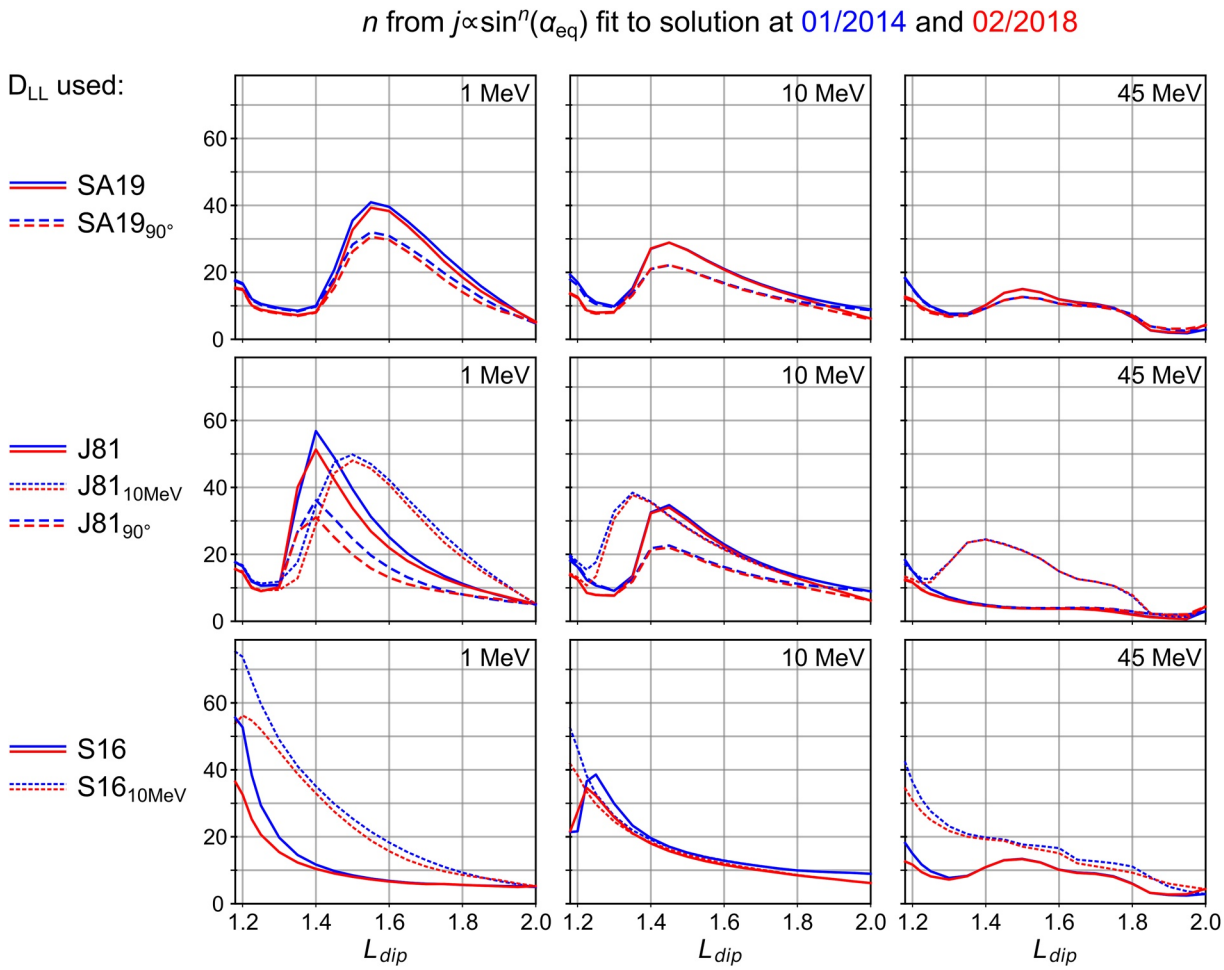

Figure 8. Pitch angle distribution anisotropy, quantified by the parameter n from the fit $j \propto \sin^n(\alpha_{eq})$, plotted against L for each of the SA19, J81 and S16 solutions (top, middle and bottom rows respectively, solid lines). Anisotropy n is plotted for 1, 10 and 45 MeV (left, middle and right columns respectively). Variations of the SA19 and J81 solutions have also been computed by modifying the corresponding D_{LL} to eliminate dependence on pitch angle (n shown by dashed lines). Additional variations of the J81 and S16 solutions have been computed by modifying the corresponding original D_{LL} to eliminate dependence on energy (n shown by dotted lines).

alongside the original results. The extra runs are labeled $SA19_{90°}$ and $J81_{90°}$ (using D_{LL} independent of pitch angle as described), and $J81_{10MeV}$ and $S16_{10MeV}$ (using D_{LL} independent of energy).

5. Discussion

Phase space density and flux levels plotted in Figures 5–7 are primarily controlled by a balance between inward transport via radial diffusion, and coulomb collisional losses to the atmosphere/ionosphere/plasmasphere. We found that variations in the CRAND source exert negligible influence over the distribution at ~MeV energy. The increase in D_{LL} from model runs SA19 to J81 to S16 hence increases the flux at lower L. Over the course of each model run, time variability arises because the balance between coulomb collisional loss and inward radial diffusion shifts. This is mostly caused by a decrease in atmospheric density, driven by a transition from solar maximum toward solar minimum, leading to increased timescales of coulomb collisional loss shown by Figure 4. Radial diffusion therefore increases phase space density by supplying protons from higher L. Changes in outer boundary flux also drive time variability, but this effect is small in the SA19 and J81 model runs except near $L = 2$.

In the S16 run, diffusion exerts more influence over time variability because the low altitude belt can be supplied with protons from higher altitude more quickly, and because changes in outer boundary flux are able to diffuse more quickly inward. This leads to the highest amount of time variability out of all the model runs, shown in

Figure 7. In contrast, variability is minimized in the SA19 run, where D_{LL} is lowest. The SA19 value of D_{LL} has no energy dependence but was applied at much lower energies than it was derived for, perhaps leading to an underestimation.

Another factor controlling the balance between coulomb collisional loss and radial diffusion is the energy range. Figure 5 shows the extent of variability is less at 50 MeV/G (right panels) compared to 20 MeV/G (left panels), and Figures 6 and 7 show the same trend, with higher variability at lower energy. This is because changes in coulomb collisional loss are more effective at lower energy where this process exerts greater influence, shown in Figure 4 by the difference in loss timescales between a 1 and 35 MeV proton. Because of this effect, we find that solar cycle variability is able to drive significant changes in flux at $L = 1.3$, shown in Figures 6 and 7 for the J81 and S16 model runs. For example, the increase in 7.5 MeV flux at $L = 1.3$ over four years is around 30% and 75% respectively for each model run. This result can be compared with work by Li et al. (2020) that indicates there is no obvious solar cycle variation at $L > 1.2$ in >36 MeV integral flux measurements made near the magnetic equator by the POES-18 satellite (Figure 6 of Li et al., 2020). As 7.5 MeV is within the key energy range responsible for solar cell degradation, this implies that solar cycle effects can also drive changes in the rate of non-ionising dose over a typical mission lifetime for a range of D_{LL}.

Figures 6 and 7 show that pitch angle distributions at $L = 1.2$ appear flat near the beginning of the modeling period, and become more peaked through time due to large increases in 90° flux. The J81 and S16 model runs both show a strong sharpening of pitch angle distributions at $L \lesssim 1.3$, but the increase in flux is significantly higher in the S16 case (Figure 7) due to the higher D_{LL}. Despite this, Figure 8 shows that anisotropy of each distribution is relatively stable throughout the duration of each model run when quantified using the fitting factor n for a fit where $j \propto \sin^n(\alpha_{eq})$. At $L = 2$, Figure 8 shows that the outer boundary evolves to become less anisotropic over the modeling period (blue to red) at ~10 MeV (center column), but this only seems to drive time variations in n at $L \gtrsim 1.7$.

Figure 8 shows significant variations in the anisotropy of pitch angle distributions across L. For example, one feature of the J81 model run is a clear increase in the anisotropy of distributions from $L = 1.3$ to 1.5 at 1–10 MeV (center panel of Figure 8, also shown in columns two and three of Figure 6). Stable n during the modeling period leads to this feature persisting over four years of time variation. However, this is somewhat at odds with a general trend suggested by previous work. For example, Figures 7a and 7b of Fischer et al. (1977) show only a decrease in n toward higher L at $L \leq 1.35$ using data at tens of MeV from the Dial satellite (collected March–May 1970, which is similar to our modeling period in terms of solar cycle). A decrease in n toward higher L is also shown in Figure 8 of Gussenhoven et al. (1993) at 36.3 MeV using data from the CRRES satellite. Figure 8 (right column) shows that our results somewhat agree with the observed trend for n to decrease with L at much higher energy (45 MeV).

One reason why our results show a trend that disagrees with previous observations at 1–10 MeV may be the steady state initialization of the proton belt. Steady state was calculated near solar maximum with high coulomb collisional loss which led to distributions being flattened at 90°, perhaps reducing anisotropy over many years. In reality, this particular balance between diffusion and loss may be too short lived to cause such changes. However, there is little data to compare with in our energy range of interest, and we therefore suggest that trends highlighted in previous literature may not be as general as expected, and may not apply at lower energy.

The extra runs presented in Figure 8 somewhat indicate the effect of pitch angle and energy dependence on anisotropy. Removing the pitch angle dependence effectively increased D_{LL} for particles at low equatorial pitch angles, and the effect is shown by comparing n between the SA19 and $SA19_{90°}$ results, as well as comparing the J81 and $J81_{90°}$ results. Anisotropy decreased at $L \sim 1.5$ when the pitch angle dependence of D_{LL} was removed, especially at lower energies, but did not change at $L \sim 1.2$. In contrast, our method of removing the energy dependence effectively led to a decrease in D_{LL} at E< 10MeV, but an increase in D_{LL} at E> 10MeV, compared with the original values. Comparing n between the J81 and $J81_{10MeV}$ results, and S16 and $S16_{10MeV}$ results, shows that removing the energy dependence did not have a consistent effect. However, the increase in D_{LL} at >10MeV generally resulted in unrealistically high values of phase space density at low L. Therefore, diffusion coefficients without energy dependence seem to be less applicable in simulations at 1–10 MeV.

6. Conclusions

We have presented physics-based calculations of proton belt phase space density and flux at $1.15 \leq L \leq 2.0$ using the 3D model BAS-PRO. Our results show variations over the ∼4 year period from 2014 to 2018, with an outer boundary driven by data derived from the RBSPICE, MagEIS and REPT instruments. We opted to investigate variations in the proton belt at low energies relevant to spacecraft solar cell degradation.

The model was applied over a coordinate range where processes known to cause variability are well constrained compared with the timescales for radial diffusion. We therefore ran simulations for three different sets of D_{LL} taken from previous literature and exhibiting various dependencies. The initial state of the proton belt was approximated as a steady state solution. An analysis of the simulation results lead to a number of conclusions:

1. We find that the proton belt is formed by inward radial diffusion from a source outside $L = 2$ balanced by coulomb collisional losses to the atmosphere, ionosphere and plasmasphere.
2. We find that the steady state solution of phase space density can vary by three orders of magnitude at $\mu = 20$ MeV/G at $L \sim 1.4$. The variation is due to uncertainty in extrapolating the radial diffusion coefficient to energies of 1–10 MeV. Since this is a very important energy range for assessing solar array degradation we suggest that more work is required to reduce the uncertainty in D_{LL}.
3. Due to the increased importance of collisional loss at low energies, solar cycle variability is able to drive up to a ∼75% increase in 7.5 MeV flux at $L = 1.3$ over four years for the D_{LL} tested, a crucial energy for solar cell degradation.
4. We find that at $L < 1.5$, certain model solutions indicate that the anisotropy of pitch angle distributions may increase toward higher L. This is somewhat at odds with previous work showing a tendency for anisotropy to decrease toward higher L. However, our results show this trend is sensitive to D_{LL}, and in particular the dependence on pitch angle.

Spacecraft measurements of flux are useful to validate theoretical calculations, but there are very few satellites equipped with detectors to measure the proton radiation belt in the 1–10 MeV energy range. However, for many spacecraft traversing the proton belt, changes in solar cell output power are dominated by the effect of proton-induced non-ionising dose affecting a fairly narrow range of energies around ∼10 MeV. In future work, we will compare solar cell output power fluctuations with theoretical calculations of degradation made using modeled flux in this energy range, in order to validate results and in turn, apply some constraints on uncertain model parameters.

Acknowledgments
The results shown in this study can be downloaded from the U.K. Polar Data Centre (at https://doi.org/10.5285/27a89a5f-ca5d-471a-a0e7-060d0911b2d1). This work was funded by the Natural Environment Research Council (NERC) via Doctoral Training Programme NE/R009457/1. Richard B. Horne and Sarah A. Glauert were supported by NERC National Capability grants NE/R016038/1 and NE/R016445/1, and by NERC grant NE/V00249X/1 (Sat-Risk), and by Highlight Topic Grant NE/P01738X/1 (Rad-Sat). Giulio Del Zanna acknowledges support from STFC (UK) via the consolidated grants to the atomic astrophysics group (AAG) at DAMTP, University of Cambridge (ST/P000665/1 and ST/T000481/1). Seth G. Claudepierre acknowledges support from NASA Grant no. NNX17AF10G and from RBSP-ECT funding provided by JHU/APL Contract 967 399 under NASA's Prime Contract NAS5-01 072. The authors thank Donald G. Mitchell and Jerry W. Manweiler for providing detailed advice on how best to process datasets from the RBSPICE instrument. The authors thank R. S. Selesnick for providing neutron albedo data to evaluate the CRAND source.

Data Availability Statement

All RBSPICE data used in this study is publicly available in the level 3 CDF files at http://rbspiceb.ftecs.com/Level_3/. The RBSPICE instrument was supported by JHU/APL Subcontract No. 937 836 to the New Jersey Institute of Technology under NASA Prime Contract No. NAS5-01 072. All MagEIS data used in this study is publicly available in the level 3 CDF files at https://rbsp-ect.newmexicoconsortium.org/data_pub/rbspb/mageis/level3/.

References

Albert, J. M., & Ginet, G. P. (1998). Crres observations of radiation belt protons: 2. time-dependent radial diffusion. *Journal of Geophysical Research*, *103*(A7), 14865–14877. https://doi.org/10.1029/98ja00290

Albert, J. M., Ginet, G. P., & Gussenhoven, M. S. (1998). Crres observations of radiation belt protons: 1. data overview and steady state radial diffusion. *Journal of Geophysical Research*, *103*(A5), 9261–9273. https://doi.org/10.1029/97ja02869

Alken, P., Thébault, E., Beggan, C. D., Amit, H., Aubert, J., Baerenzung, J., et al. (2021). International geomagnetic reference field: The thirteenth generation. *Earth, Planets and Space*, *73*(1), 1–25. https://doi.org/10.1186/s40623-020-01288-x

Baker, D. N., Kanekal, S. G., Hoxie, V. C., Batiste, S., Bolton, M., Li, X., et al. (2012). The relativistic electron-proton telescope (REPT) instrument on board the radiation belt storm probes (RBSP) spacecraft: Characterization of earth's radiation belt high-energy particle populations. *Space Science Reviews*, *179*(1–4), 337–381. https://doi.org/10.1007/s11214-012-9950-9

Beutier, T., Boscher, D., & France, M. (1995). Salammbo: A three-dimensional simulation of the proton radiation belt. *Journal of Geophysical Research*, *100*(A9), 17181–17188. https://doi.org/10.1029/94ja02728

Bilitza, D., Altadill, D., Truhlik, V., Shubin, V., Galkin, I., Reinisch, B., & Huang, X. (2017). International reference ionosphere 2016: From ionospheric climate to real-time weather predictions. *Space Weather*, *15*(2), 418–429. https://doi.org/10.1002/2016sw001593

Blake, J. B., Carranza, P. A., Claudepierre, S. G., Clemmons, J. H., Crain, W. R., Dotan, Y., et al. (2013). The magnetic electron ion spectrometer (MagEIS) instruments aboard the radiation belt storm probes (RBSP) spacecraft. In *The van Allen probes mission* (pp. 383–421). Springer US. https://doi.org/10.1007/978-1-4899-7433-4_12

Decker, B. L. (1986). World geodetic system 1984. In *Fourth International Geodetic Symposium on Satellite Positioning* (Vol. AD-A167 570. p. 22). University of Texas. Retrieved from https://apps.dtic.mil/dtic/tr/fulltext/u2/a167570.pdf

Dragt, A. J., Austin, M. M., & White, R. S. (1966). Cosmic ray and solar proton albedo neutron decay injection. *Journal of Geophysical Research*. *71*(5), 1293–1304. https://doi.org/10.1029/jz071i005p01293

Fälthammar, C.-G. (1965). Effects of time-dependent electric fields on geomagnetically trapped radiation. *Journal of Geophysical Research*, *70*(11), 2503–2516. https://doi.org/10.1029/jz070i011p02503

Farley, T. A., & Walt, M. (1971). Source and loss processes of protons of the inner radiation belt. *Journal of Geophysical Research*, *76*(34), 8223–8240. https://doi.org/10.1029/ja076i034p08223

Fischer, H. M., Auschrat, V. W., & Wibberenz, G. (1977). Angular distribution and energy spectra of protons of energy $5 \leq e \leq 50$ mev at the lower edge of the radiation belt in equatorial latitudes. *Journal of Geophysical Research*, *82*(4), 537–547. https://doi.org/10.1029/ja082i004p00537

Fuller-Rowell, T., Solomon, S., Roble, R., & Viereck, R.. Impact of solar euv, xuv, and x-ray variations on earths's atmosphere. *Geophysical Monograph Series*, *141*. https://doi.org/10.1029/141GM23

Ginet, G. P., O'Brien, T. P., Huston, S. L., Johnston, W. R., Guild, T. B., Friedel, R., et al. (2013). AE9, AP9 and SPM: New models for specifying the trapped energetic particle and space plasma environment. In *The van allen probes mission* (pp. 579–615). Springer US. https://doi.org/10.1007/978-1-4899-7433-4_18

Gussenhoven, M., Mullen, E., Violet, M., Hein, C., Bass, J., & Madden, D. (1993). Crres high energy proton flux maps. *IEEE Transactions on Nuclear Science*, *40*(6), 1450–1457. https://doi.org/10.1109/23.273519

Hudson, M. K., Kotelnikov, A. D., Li, X., Roth, I., Temerin, M., Wygant, J., et al. (1995). Simulation of proton radiation belt formation during the march 24, 1991 ssc. *Geophysical Research Letters*, *22*(3), 291–294. https://doi.org/10.1029/95gl00009

Jenkins, P. P., Bentz, D. C., Barnds, J., Binz, C. R., Messenger, S. R., Warner, J. H., et al. (2014). Tacsat-4 solar cell experiment: Two years in orbit. In *10th European Space Power Conference, Noordwijkerhout*, Netherlands (Vol. 14).

Jentsch, V. (1981). On the role of external and internal source in generating energy and pitch angle distributions of inner-zone protons. *Journal of Geophysical Research: Space Physics*, *86*(A2), 701–710. https://doi.org/10.1029/ja086ia02p00701

Kessel, R., Fox, N., & Weiss, M. (2013). The radiation belt storm probes (rbsp) and space weather. *Space Science Reviews*, *179*(1–4), 531–543. https://doi.org/10.1007/978-1-4899-7433-4_16

Kovtyukh, A. S. (2016). Deduction of the rates of radial diffusion of protons from the structure of the earth's radiation belts. *Annales Geophysicae*, *34*(11), 1085–1098. https://doi.org/10.5194/angeo-34-1085-2016

Kress, B. T., Hudson, M. K., Perry, K. L., & Slocum, P. L. (2004). Dynamic modeling of geomagnetic cutoff for the 23–24 november 2001 solar energetic particle event. *Geophysical Research Letters*, *31*(4). https://doi.org/10.1029/2003gl018599

Kress, B. T., Hudson, M. K., & Slocum, P. L. (2005). Impulsive solar energetic ion trapping in the magnetosphere during geomagnetic storms. *Geophysical Research Letters*, *32*(6). https://doi.org/10.1029/2005gl022373

Lejosne, S. (2019). Analytic expressions for radial diffusion. *Journal of Geophysical Research: Space Physics*, *124*, 4278–4294. https://doi.org/10.1029/2019ja026786

Lejosne, S., Boscher, D., Maget, V., & Rolland, G. (2013). Deriving electromagnetic radial diffusion coefficients of radiation belt equatorial particles for different levels of magnetic activity based on magnetic field measurements at geostationary orbit. *Journal of Geophysical Research: Space Physics*, *118*, 3147–3156. https://doi.org/10.1002/jgra.50361

Lejosne, S., & Kollmann, P. (2020). Radiation belt radial diffusion at earth and beyond. *Space Science Reviews*, *216*(1). https://doi.org/10.1007/s11214-020-0642-6

Letaw, J. R., Silberberg, R., & Tsao, C. H. (1983). Proton-nucleus total inelastic cross sections - An empirical formula for E greater than 10 MeV. *Astrophysical Journal Supplement Series*, *51*, 271–275. https://doi.org/10.1086/190849

Li, X., Selesnick, R., Schiller, Q., Zhang, K., Zhao, H., Baker, D. N., & Temerin, M. A. (2017). Measurement of electrons from albedo neutron decay and neutron density in near-earth space. *Nature*, *552*(7685), 382–385. https://doi.org/10.1038/nature24642

Li, X., Xiang, Z., Zhang, K., Khoo, L., Zhao, H., Baker, D. N., & Temerin, M. A. (2020). New insights from long-term measurements of inner belt protons (10s of mev) by sampex, poes, van allen probes, and simulation results. *Journal of Geophysical Research: Space Physics*, *125*, e2020JA028198. https://doi.org/10.1029/2020ja028198

Lorentzen, K. R., Mazur, J. E., Looper, M. D., Fennell, J. F., & Blake, J. B. (2002). Multisatellite observations of mev ion injections during storms. *Journal of Geophysical Research*, *107*(A9). https://doi.org/10.1029/2001ja000276

Lozinski, A. R., Horne, R. B., Glauert, S. A., Del Zanna, G., & Albert, J. M. (2021). Optimization of radial diffusion coefficients for the proton radiation belt during the crres era. *Journal of Geophysical Research: Space Physics*, *126*, e2020JA028486. https://doi.org/10.1029/2020ja028486

Manweiler, J. W., & Mull, H. (2017). *Rbspice science data handbook (revision:[Computer software manual]*. Retrieved from http://rbspice.ftecs.com/RBSPICE%20Data%20Handbook_Rev_d.htm

Meyer, J. P. (1972). Deuterons and He^3 formation and destruction in proton induced spallation of light nuclei ($Z \leq 8$). *Astronomy and Astrophysics Supplement*, *7*, 417.

Mitchell, D. G., Lanzerotti, L. J., Kim, C. K., Stokes, M., Ho, G., Cooper, S., et al. (2013). Radiation belt storm probes ion composition experiment (RBSPICE). In *The van Allen probes mission* (pp. 263–308). Springer US. https://doi.org/10.1007/978-1-4899-7433-4_8

Miyake, W., Miyoshi, Y., & Matsuoka, A. (2014). On the spatial extent of the proton radiation belt from solar cell output variation of the akebono satellite. *Advances in Space Research*, *53*(11), 1603–1609. https://doi.org/10.1016/j.asr.2014.03.002

Morley, S. K., Koller, J., Welling, D. T., Larsen, B. A., Henderson, M. G., & Niehof, J. T. (2011). Spacepy - A python-based library of tools for the space sciences. In *Proceedings of the 9th python in science conference (scipy 2010)*. Austin, TX.

Olson, W. P., & Pfitzer, K. A. (1982). A dynamic model of the magnetospheric magnetic and electric fields for july 29, 1977. *Journal of Geophysical Research*, *87*(A8), 5943–5948. https://doi.org/10.1029/ja087ia08p05943

Ozhogin, P., Tu, J., Song, P., & Reinisch, B. W. (2012). Field-aligned distribution of the plasmaspheric electron density: An empirical model derived from the image rpi measurements. *Journal of Geophysical Research*, *117*. https://doi.org/10.1029/2011ja017330

Park, C. G., Carpenter, D. L., & Wiggin, D. B. (1978). Electron density in the plasmasphere: Whistler data on solar cycle, annual, and diurnal variations. *Journal of Geophysical Research*, *83*(A7), 3137–3144. https://doi.org/10.1029/ja083ia07p03137

Parker, E. N. (1960). Geomagnetic fluctuations and the form of the outer zone of the van Allen radiation belt. *Journal of Geophysical Research*, *65*(10), 3117–3130. https://doi.org/10.1029/jz065i010p03117

Picone, J. M., Hedin, A. E., Drob, D. P., & Aikin, A. C. (2002). Nrlmsise-00 empirical model of the atmosphere: Statistical comparisons and scientific issues. *Journal of Geophysical Research*, *107*(A12). https://doi.org/10.1029/2002ja009430

Schulz, M. (1991). The magnetosphere. In *Geomagnetism* (pp. 87–293). Elsevier. https://doi.org/10.1016/b978-0-12-378674-6.50008-x

Schulz, M., & Lanzerotti, L. (1974). Physics and chemistry in space. *Particle Diffusion in the Radiation Belts*, *7*.

Selesnick, R. S., & Albert, J. M. (2019). Variability of the proton radiation belt. *Journal of Geophysical Research: Space Physics*, *124*(7), 5516–5527. https://doi.org/10.1029/2019ja026754

Selesnick, R. S., Baker, D. N., Jaynes, A. N., Li, X., Kanekal, S. G., Hudson, M. K., & Kress, B. T. (2014). Observations of the inner radiation belt: Crand and trapped solar protons. *Journal of Geophysical Research: Space Physics*, *119*, 6541–6552. https://doi.org/10.1002/2014ja020188

Selesnick, R. S., Baker, D. N., Jaynes, A. N., Li, X., Kanekal, S. G., Hudson, M. K., & Kress, B. T. (2016). Inward diffusion and loss of radiation belt protons. *Journal of Geophysical Research: Space Physics*, *121*, 1969–1978. https://doi.org/10.1002/2015ja022154

Selesnick, R. S., Looper, M. D., & Mewaldt, R. A. (2007). A theoretical model of the inner proton radiation belt. *Space Weather*, *5*(4). https://doi.org/10.1029/2006sw000275

Singer, S. F. (1958). Trapped albedo theory of the radiation belt. *Physical Review Letters*, *1*(5), 181. https://doi.org/10.1103/physrevlett.1.181

Smart, D., & Shea, M. (2005). A review of geomagnetic cutoff rigidities for earth-orbiting spacecraft. *Advances in Space Research*, *36*(10), 2012–2020. https://doi.org/10.1016/j.asr.2004.09.015

Stassinopoulos, E., & Raymond, J. (1988). The space radiation environment for electronics. *Proceedings of the IEEE*, *76*(11), 1423–1442. https://doi.org/10.1109/5.90113

Walt, M. (1971). The radial diffusion of trapped particles induced by fluctuating magnetospheric fields. *Space Science Reviews*, *12*(4), 446–485. https://doi.org/10.1007/BF00171975